Metamorphic evolution of the Tethyan Himalayan flysch in SE Tibet

I. DUNKL[1]*, B. ANTOLÍN[2], K. WEMMER[1], G. RANTITSCH[3], M. KIENAST[1], C. MONTOMOLI[4], L. DING[5], R. CAROSI[4], E. APPEL[2], R. EL BAY[2], Q. XU[5] & H. VON EYNATTEN[1]

[1]*Geoscience Center, University of Göttingen, Goldschmidtstrasse 3, D-37077 Göttingen, Germany*

[2]*Institute for Geosciences, University of Tübingen, Sigwartstrasse 10, D-72076 Tübingen, Germany*

[3]*University of Leoben, Peter-Tunner-Straße 5, A-8700 Leoben, Austria*

[4]*Department of Earth Sciences, University of Pisa, via S. Maria 53, I-56126 Pisa, Italy*

[5]*Institute of Tibetan Plateau Research, Chinese Academy of Sciences, Shuangqing Road 18, Beijing 100085, China*

**Corresponding author (e-mail: istvan.dunkl@geo.uni-goettingen.de)*

Abstract: The metamorphic conditions and the age of thermal overprint were determined in metapelites, metaarenites and metabasites of the Tethyan Himalayan Sequence (THS) in SE Tibet using Kübler Index and vitrinite reflectance data and applying thermobarometrical (Thermocalc and PERPLEX) and geochronological methods (illite/muscovite K–Ar and zircon and apatite (U–Th)/He chronology). The multiple folded thrust pile experienced a thermal overprint reaching locally peak conditions between the diagenetic stage (*c.* 170 °C) and the amphibolite facies (*c.* 600 °C at 10 kbar). Burial diagenesis and heating due to Early Cretaceous dyke emplacement triggered the growth of illite in the metapelites. Eocene collision-related peak metamorphic conditions have been reached at *c.* 44 Ma. During collision the different tectonic blocks of the THS were tectonically buried to different structural levels so that they experienced maximum greenschist to amphibolite facies metamorphism. Later, during Oligocene to Miocene times the entire THS underwent anchi- to epizonal metamorphic conditions, probably associated to continuous deformation in the flysch fold-thrust-system. This period terminated at *c.* 24–22 Ma. Adjacent to the north Himalayan metamorphic domes, the base of the THS was metamorphosed during Miocene times (*c.* 13 Ma). Post-metamorphic cooling below *c.* 180 °C lasted until Late Miocene and took place at different times.

The northward drift of Greater India during the Cenozoic resulted in the closure of the Tethys ocean, the initiation of the India–Asia collision in the Paleocene and the subsequent uplift of the Himalayan Range (*c.* 55–50 Ma; e.g. Gaetani & Garzanti 1991; Patzelt *et al.* 1996; Najman *et al.* 2005). The Himalayan arc forms an active WNW–ESE asymmetric fold and thrust belt with a main southward vergence (Fig. 1a, b). The northern member of the Himalaya is the Tethyan Himalayan Sequence (THS) which is located in the highest structural position within the orogen (Le Fort 1975; Hodges 2000). For that reason the rocks forming the THS have probably better preserved the early tectonothermal evolution of the Himalayan orogen than other tectonometamorphic units, like the Greater Himalayan Sequence, made up by mid-crustal rocks which has nearly lost its pre-climax memory during metamorphism around 23–17 Ma (Guillot *et al.* 1993; Harrison *et al.* 1997; Searle & Godin 2003; Godin *et al.* 2006).

The THS can be traced along the 2500 km of the Himalayan arc between the Nanga Parbat syntaxis in the west and the Namche Barwa syntaxis in the east (Fig. 1). The Cambrian to Eocene sequence is composed of very variable lithologies, derived from different sedimentary facies zones of the former passive continental margin of the Indian plate (e.g. Brookfield 1993; Willems *et al.* 1996; Garzanti 1999). Some tectonic domains are altered only diagenetically and usually low-grade metamorphism was not exceeded (e.g. Fuchs 1967; Hodges *et al.* 1996; Crouzet *et al.* 2007).

The aim of this study is to constrain the post-sedimentary evolution of the THS from metamorphic and geochronological data. In the study

From: GLOAGUEN, R. & RATSCHBACHER, L. (eds) *Growth and Collapse of the Tibetan Plateau.* Geological Society, London, Special Publications, **353**, 45–69.
DOI: 10.1144/SP353.4 0305-8719/11/$15.00

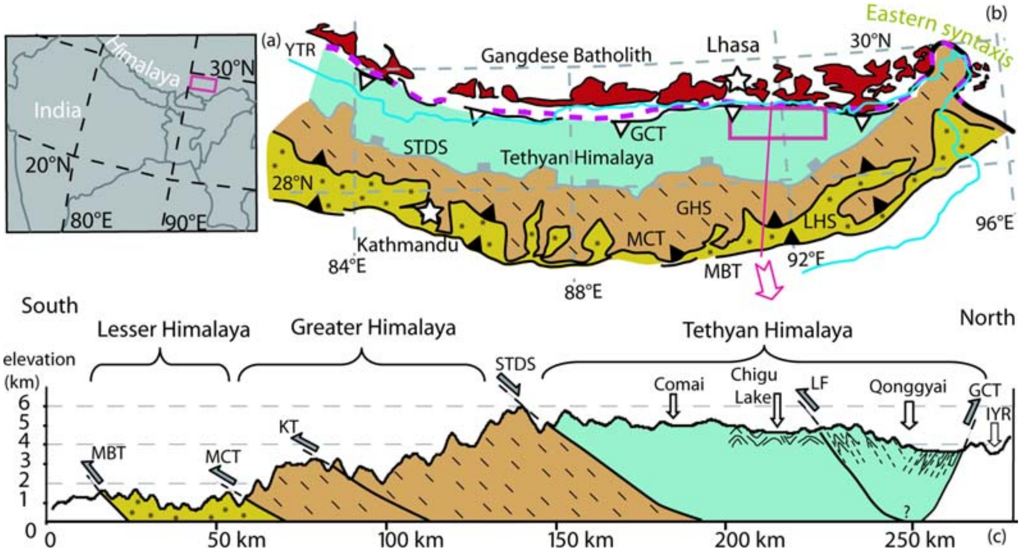

Fig. 1. (**a**) Position of the study area in SE Tibet (red box). (**b**) Major structural units of Central and Eastern Himalayas. The study area (red box, see Fig. 2) situated close to the eastern termination of Tethyan Himalayan Sequence. Violet dashed line shows the Indus-Yarlung suture zone; YTR, Yarlung Tsangpo River; GCT, Great Counter Thrust; STDS, South Tibetan Detachment System; GHS, Greater Himalayan Sequence; MCT, Main Central Thrust; LHS, Lesser Himalayan Sequence; MBT, Main Boundary Thrust (simplified after Pan *et al.* 2004; Yin 2006). (**c**) Schematic cross section along the red line in Figure 1b. KT, Kakhtang thrust, position of STDS from Grujic *et al.* (2002), McQuarrie *et al.* (2008). Structures in the northern Tethyan Himalaya from Antolin *et al.* (2011).

area (Fig. 1b) previous metamorphic and geochronological studies have been focused mainly on the Indus-Yarlung suture zone, Great Counter Thrust and Gangdese Thrust (e.g. Yin *et al.* 1994; Quidelleur *et al.* 1997; Harrison *et al.* 2000; Dupuis *et al.* 2005). However our studied profiles are distributed along valleys south of the Indus-Yarlung Suture where few work has been done before.

Kübler Index (KI) for 'illite crystallinity', vitrinite reflectance data, and K–Ar dating of micron and sub-micron fractions of illite are used to constrain the degree and age of metamorphism on metapelites, slates and sandstones of the Triassic flysch, which is the dominant metasedimentary sequence of the eastern THS. Thermobarometric methods (Thermocalc and PERPLEX, Holland & Powell 1998; Connolly & Petrini 2002, respectively) were applied on metamorphosed basic dyke rocks, which experienced a greenschist to amphibolite facies overprint.

Geological setting

The major tectonic structures in the Himalayan Range are from south to north, the Himalaya Frontal Thrust (HFT), the Main Boundary Thrust (MBT), the Main Central Thrust (MCT), the South Tibetan Detachment System (STDS), the Great Counter Thrust (GCT) and the Indus-Yarlung Suture Zone (IYSZ; Fig. 1b, c; Hodges 2000; Upreti 2001 and references therein; Yin 2006). These structural discontinuities divide the Himalaya into three main units traceable along the entire mountain belt. The Lesser Himalayan sequence between MBT and MCT is composed of Proterozoic–Cambrian sediments deposited on the proximal Indian shelf. Paleocene sediments are found in the eastern part of the belt (Stöcklin 1980; Valdiya 1980). This sequence was deformed by thrust and folds under very low-grade metamorphic conditions (Le Fort 1975; DeCelles *et al.* 2001; Robinson *et al.* 2003; Paudel & Arita 2006). The Greater Himalayan Sequence (GHS) in the hanging wall of the north-dipping MCT consists of high grade meta-sediments, meta-igneous rocks (Le Fort 1971; Pêcher 1975; Grujic *et al.* 2002) and leucogranitic intrusions in the footwall of the STDS (e.g. Guillot *et al.* 1993; Searle & Godin 2003). The uppermost unit, the Tethyan Himalayan Sequence is bordered by STDS and GCT and forms the cover of the Greater Himalayan Sequence. The middle part of the THS is characterized by the outcrop of the North Himalayan gneiss domes, which contains leucogranite bodies of Early Miocene age (e.g. Lee *et al.* 2000; Leech 2008).

The Tethyan Himalayan Sequence

The Tethyan Himalayan Sequence involves a Cambro-Ordovician to Eocene pile that crops out along *c.* 150 km between STDS and IYSZ (Fig. 1; Brookfield 1993; Pan *et al.* 2004), deposited on the passive northern margin of the Indian continent (Fuchs 1967; Willems *et al.* 1996; Garzanti 1999). The Gyrong-Kangmar thrust in south–central Tibet divides the Tethyan Himalaya into two sub-units (Liu & Einsele 1994). The southern sub-unit, north of the STDS, is formed by more than 13 km thick Cambrian to Eocene carbonates of the former passive margin, whereas the northern sub-unit is composed of Cretaceous clastic sediments recording the separation of the Indian plate from Gondwana and the drift to abyssal conditions (Willems *et al.* 1996). Towards the east, in SE Tibet, Lhunze fault (Fig. 2) separates the passive palaeomargin into two sub-units (Pan *et al.* 2004; Aikman *et al.* 2008). South of it, the Tethyan sediments are composed of Cretaceous clastic rocks, Jurassic–Cretaceous marine clastic rocks intercalated with intermediate–basic volcanic rocks, and marine limestones in the hanging wall of the STDS (Fig. 2; Pan *et al.* 2004). The sub-domain north of the Lhunze fault is build up by turbiditic sandstones and slates – subsequently called as flysch sequence. It was deposited in abyssal and bathyal environments between Middle Triassic and Early Jurassic (Mercier *et al.* 1984; Pan *et al.* 2004; Dupuis *et al.* 2005). In the north the flysch is juxtaposed against rocks of the active palaeomargin (Lhasa block), ophiolites related to the IYSZ and the mélange complex (Heim & Gansser 1939; Ratschbacher *et al.* 1994; Yin *et al.* 1994; Quidelleur *et al.* 1997). The mélange complex (limestones, cherts, marbles, shales, phyllites, andesites, diorites, mafic and ultramafic bodies) was deposited on the growing Neo-Tethys ocean floor (e.g. Searle 1986). The southern border of the Lhasa block is made up of Cretaceous clastic rocks and the Gangdese granite (Yin *et al.* 1994; Harrison *et al.* 2000; Pan *et al.* 2004). Ophiolites are widespread distributed along the suture and related to a supra-subduction environment (Ding *et al.* 2005; Dupuis *et al.* 2005, 2006).

Mafic magmatism

In SE Tibet the Tethyan flysch sequence is penetrated by basalt, diabase, gabbroic diabase, diorite, olivine websterite and lherzolite dykes (Zhu *et al.* 2008; Xu *et al.* 2009). The silica content is typically between 43–55%. The thickness of the dykes is variable; it ranges from a few metres to *c.* 100 m. The texture and the typical crystal size are also very variable from fine grained, nearly aphanitic to very coarse-grained holocrystalline. In the ultramafic members poikilitic or cummulate textures are typical. According to zircon SHRIMP U–Pb geochronology the dykes intruded 145–130 Ma ago (Xu *et al.* 2009). Some of the magmatic bodies and typically their interior parts show well preserved magmatic textures, but in many occurrences the dykes are strongly deformed and transformed to chlorite or amphibole schists. The dykes form usually dissected boudins; the margins and the contact aureoles of the dykes are mainly detached or altered to banded, chaotic, mica-rich zones.

Structural setting of the Tethyan Himalaya

The entire Tethyan sequence has been folded and imbricated during several tectonic phases. In the southern sector of the study area the main deformation phase (Eohimalayan phase: Hodges 2000) is related to the Middle Eocene to Late Oligocene collision of India against Asia. It is characterized by top-to-the-south thrust faults and south-facing folds (e.g. Burg & Chen 1984; Ratschbacher *et al.* 1994; Carosi *et al.* 2007; Aikman *et al.* 2008; Montomoli *et al.* 2008, Antolin *et al.* 2011). During the subsequent Neohimalayan (Hodges 2000) tectonic phase, north-facing folds with a related axial plane cleavage were developed (e.g. Carosi *et al.* 2007; Montomoli *et al.* 2008; Kellett & Godin 2009, Antolin *et al.* 2011). In the study area these two deformation phases are well developed. The first one is widespread in the southern sector, whereas the second one is well-developed in the northern portion. Consequently, two structural domains have been distinguished by Montomoli *et al.* (2008) and Antolin *et al.* (2011).

Both deformation phases (D1 and D2) are associated to folds (F1 and F2 respectively) with related axial plane foliations (S1 and S2). The S1 foliation is associated to a synkinematic recrystallization of chlorite, white mica, calcite, quartz and oxides. The strain of the D2 phase increases progressively towards the north at the point that S2 foliation transposes the S1 foliation in the northern more strained areas. S2 foliation is a crenulation cleavage in the southern sector with no dynamic recrystallization, whereas in the north, it is associated to dynamic recrystallization of chlorite, white mica, calcite, quartz and oxides (Montomoli *et al.* 2008; Antolin *et al.* 2011).

Godin (2003) used cross-cutting relationships of the different structural elements and U–Pb geochronology to date the D2 fold structures in the Annapurna area as Oligocene. In central Nepal Crouzet *et al.* (2007) dated the D2 tectonic phase by K–Ar ages of newly formed illite with *c.* 30–25 Ma. The synchronous activity of the STDS and the MCT along the Himalayan arc resulted in the exhumation

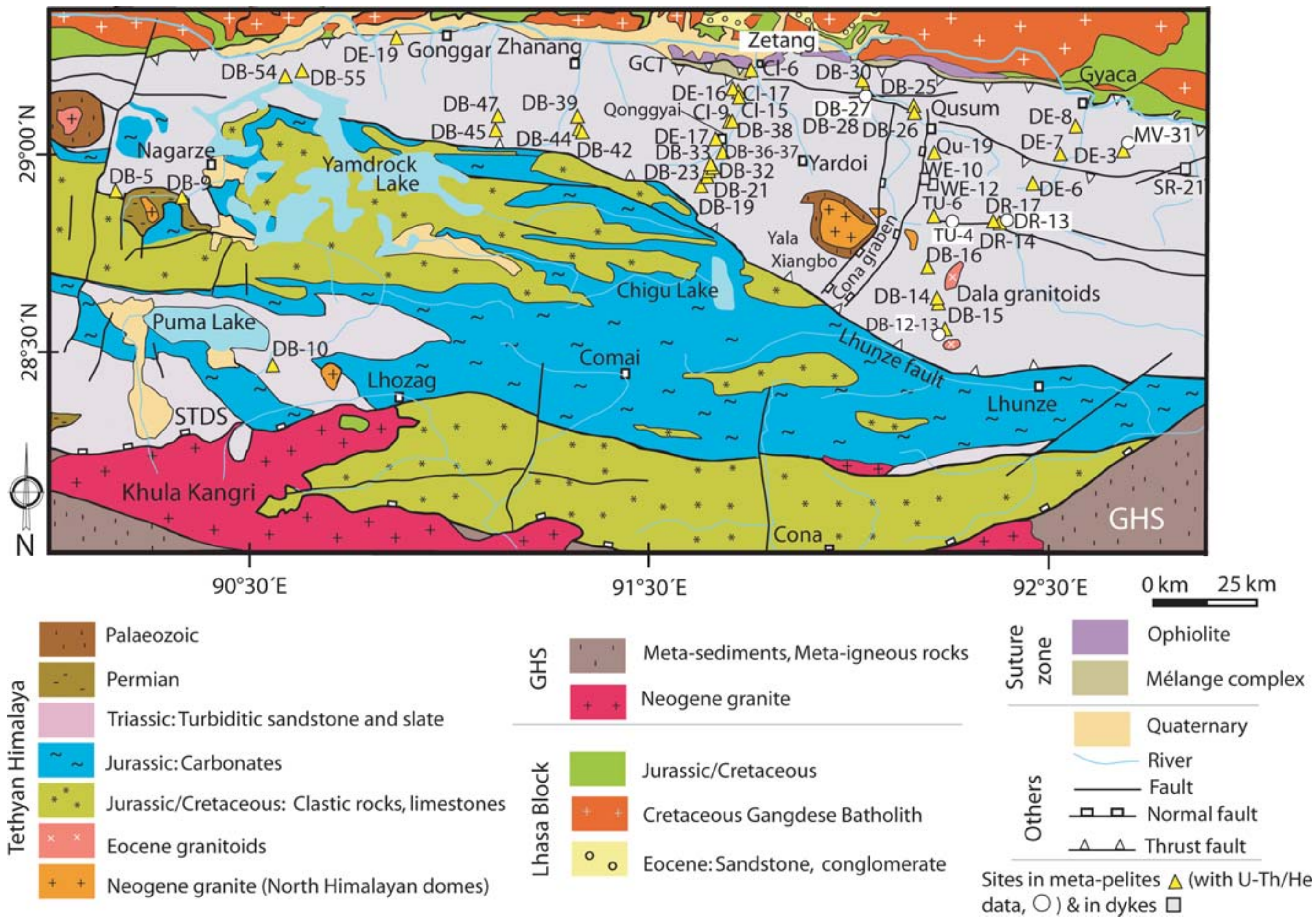

Fig. 2. Simplified geological map of SE Tibet (after Pan *et al.* 2004; Yin, 2006; Aikman *et al.* 2008; Antolin *et al.* 2011).

of mid-crustal rocks of the GHS *c*. 23–17 Ma ago (Godin *et al.* 2006 with references). By Th–Pb ion microprobe dating on monazite grains from the Khula Kangri granite, the age of activity of the STDS was dated to be younger than 12.5 Ma in the Eastern Himalaya (Fig. 2; Edwards & Harrison 1997). The displacement along the MCT in the western Arunachal Pradesh was dated to be *c*. 10 Ma by U–Th ion microprobe dating of monazite inclusions in synkinematic garnets (Yin 2006). During this time interval, the northern part of the Tethyan Himalaya was thrust along the GCT to the north at about 17 Ma in the south–central Tibet and between 18–10 Ma near Zetang (Fig. 2; Ratschbacher *et al.* 1994; Harrison *et al.* 2000). The final tectonic phase took place during Miocene times when orogen parallel (east–west) extension triggered north–south-trending normal faults in form of graben structures, cross-cutting both the Lhasa block and the Tethyan Himalaya. In the study area related structures are formed by the Yadong Gulu Graben at the western margin of the study area and the Cona Graben at longitude of *c*. 92°E (Fig. 2; Armijo *et al.* 1986; Garzione *et al.* 2003).

Samples

The study area is situated south and SE of Lhasa along a 250 km long stripe where the Triassic flysch of the Tethyan sediments form the widest belt in the Himalayan chain (Figs 1 & 2). The present study focuses on north–south profiles along valleys between Nagarze in the west (90°20′E) and Gyaca in the east (92°50′E). From west–east, the main studied valleys are given by the name of the major localities (length of the profile in brackets): Nagarze (85 km), Zetang (45 km), Qusum (70 km) and Gyaca (17 km). 203 samples were collected from metapelites and arenites of the Triassic flysch sequence, from the basaltic–dioritic dykes, and greenschists formed from these magmatic rocks.

The metapelites are typically dark grey to black with a total organic carbon content of 2–4 wt% and a sulphur content of 0.01–0.3 wt%. They are rich in early diagenetic pyrite cubes with crystal size up to 2 cm. Sandstone layers (grey, well-sorted quartz-litharenites, with some wackes and red quartzites) are widespread in the sequence. The deformation of the flysch assemblage varies strongly along north–south profiles (e.g. Montomoli *et al.* 2008; Antolin *et al.* 2011) and the post-sedimentary overprint ranges from the diagenetic stage to greenschist and amphibolite facies. Thus, microscopic textures and mineral assemblages of samples from different structural domains vary from purely sediment to completely recrystallized schists (see Fig. 3a–d).

The mafic–intermediate magmatites usually form several metres wide dykes or house-sized, dissected boudins. They experienced a very variable degree of deformation. In the internal zones of the coarsest gabbro and diorite bodies even primary mafic minerals are well preserved, but the margins of the magmatic bodies commonly show transformation to chlorite–muscovite schist. In tectonic units where the degree of metamorphism is high penetrative, ductile deformation is widespread and the entire volumes of the magmatites were transformed to greenschist or amphibole–garnet schist (see Fig. 3e, f).

Methods

Kübler index ('illite crystallinity')

For Kübler index (KI) estimation and K–Ar dating, the fractions <0.2, <2 and 2–6 μm nominal size were separated from fine grained, pelitic–silty samples as follows. After crushing the samples to *c*. 1 cm size, only homogeneous, fine-grained rock fragments, completely free of limonite staining, detrital mica flakes and calcite or quartz veins were selected. The hand-picked aliquots were crushed and ground in a ring mill (vibration mill equipped by hard metal inlays) for 10 to 20 s, sieved and split into two parts. The <63 μm fractions were used to extract the illite-rich fractions of <2 μm by settling in Atterberg cylinders. A second aliquot of <2 μm fraction was used to separate the fraction <0.2 μm by an ultra-centrifuge. Due to the coarse crystal size of newly grown mica, it was not possible to produce a sufficient amount of <0.2 μm fraction in samples with a relatively high degree of metamorphism. From these samples the <2 and 2–6 μm fractions were investigated. The mineralogical composition of all fine aliquots was examined by X-ray diffraction.

The KI is the half height peak width of the 10-Å illite peak in X-ray diffractograms (Kübler 1990). Digital measurement of KI was carried out by step scanning (301 points between 7–10° 2Θ, with scan steps of 0.010° 2Θ, integration time 4 s, receiving slit 0.1 mm, automatic divergence slit) on a Philips PW 1800 diffractometer. The KI values were calculated by the IDEFIX computer program developed at the Geoscience Centre of the University of Göttingen by D. Friedrich and was rewritten to FORTRAN by K. Ullemeyer (Geomar, Kiel) in 2005. To detect the expandable layers of mixed-layer minerals, measurements were carried out in 'air dry' and 'glycolated' state of the size fractions. All samples were investigated in duplicates, and the KI-values are given in Δ°2Θ as an average of the two measurements. As suggested by Kübler (1967, 1968, 1990) the anchizone is limited by 0.25 and

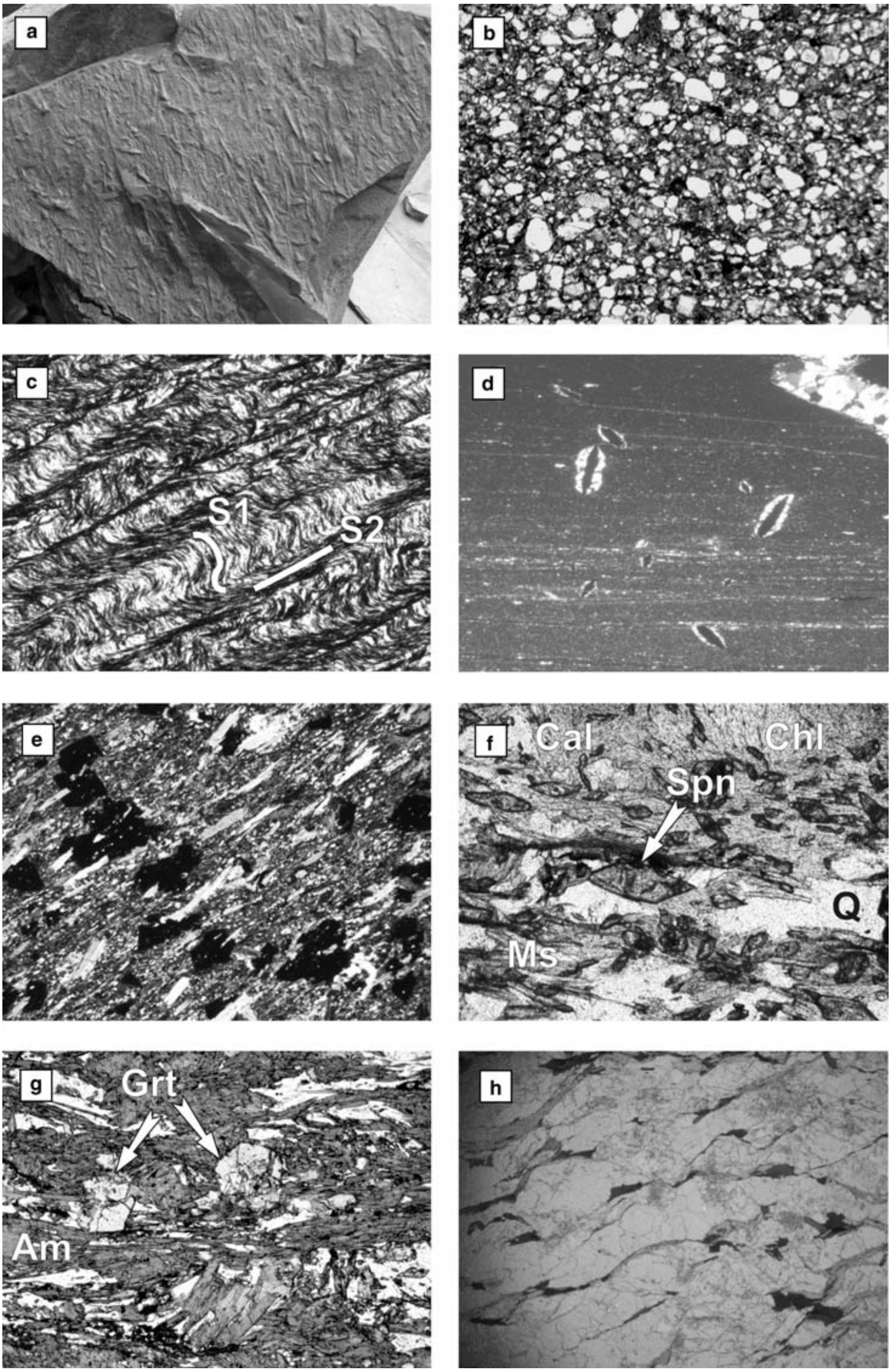

Fig. 3. Macroscopic images and microphotographs demonstrating the characteristic textures and the mineral assemblages of the Tethyan (meta)flysch sequence. (**a**) Bottom-view of the bedding surface of a sandstone layer from the less deformed, southernmost zone of the sequence, which experienced only diagenetic overprint (site DB-19).

0.42 $\Delta°2\theta$, respectively. The used methodology has been validated by an inter-laboratory standardization program (see e.g. Warr & Rice 1994; Kisch *et al.* 2004; Árkai *et al.* 2007).

Vitrinite reflectance

Apparent maximum, minimum (R_{max}, R_{min}) and random vitrinite reflectances (R_r) were measured on polished sections cut perpendicular to the foliation, using polarized light and plane polarized light, respectively. The measurements were carried out at wavelength of 546 nm. Reflection was recorded on fine-dispersed vitrinite particles characterized by an elongated shape, smooth surface and strong bireflectance, without any traces of oxidation and/or re-deposition.

Thermobarometry

Petrographic thin sections were polished, carbon coated and analysed using a JEOL JXA 8900 electron microprobe. A tungsten filament was used as electron source. The acceleration voltage for quantitative wave length dispersive spot analyses and line scans was set to 15 kV. The beam current was adjusted to 15 nA with a beam diameter of 5 µm. The count time for the peak position for each element was 15 s. The lower and upper background was measured for 5 s each. A Phi–Rho Z matrix correction was applied on all measurements (Armstrong 1991). The following phases were used as standards for the analysed elements: olivine_SC, albite, sanidine, TiO_2, hematite, anorthite, wollastonite, rhodonite, Cr_2O_3 and NiO.

The pressure and temperature (pT) conditions for samples WE-12 and Sr-21-a were calculated with Thermocalc (Holland & Powell 1998; Powell & Holland 2006) were obtained using the average pT mode or *avpT*. The PC Version 3.32 of Thermocalc with the internally consistent dataset tc-ds55s, obtained from the Thermocalc resource page (http://www.metamorph.geo.uni-mainz.de/thermocalc/index.html) was used. To convert the mineral compositions into chemical activities the program AX, by T. J. B. Holland (http://rock.esc.cam.ac.uk/astaff/holland/index.html) was used. After each run of Thermocalc the activities of the phases were iteratively recalculated with AX. This was done until a best fit between the pT results of Thermocalc and the calculation conditions for AX was achieved. The crucial σ_{fit} value of the avpT mode of Thermocalc (Powell & Holland 2006) was observed during the calculations. The quoted pT values are within the σ_{fit} range.

The computer program PERPLEX (Connolly & Petrinin 2002; Connolly 2005) was applied to construct a phase diagram section or pseudosections (Powell & Holland 2008) of sample SR-21-a. The pseudosection was utilized to plot the garnet composition isopleths of the four garnet end members (almandine, pyrope, grossularite and spessartine). The necessary chemical information was obtained with a whole rock XRF analyses as well as electron microprobe spot analyses of garnet cores. The intersection of four isopleths yields the range of pT conditions during the initial growth period of the garnets. This approach is discussed by J. A. D. Connolly on the PERPLEX resource page (http://www.perplex.ethz.ch/perplex_pseudosection.html).

K–Ar geochronology

The argon isotopic composition was measured in a Pyrex glass extraction and purification line coupled to a VG 1200 C noble gas mass spectrometer operating in static mode. The amount of radiogenic ^{40}Ar is determined by isotope dilution method using a highly enriched ^{38}Ar spike from Schumacher, Bern (Schumacher 1975). The spike is calibrated against the biotite standard HD-B1 (Fuhrmann *et al.* 1987). The age calculations are based on the constants recommended by the IUGS quoted in Steiger & Jäger (1977). Potassium is determined in duplicate by Eppendorf Elex 63/61 flame photometer. The samples are dissolved in a mixture of HF and HNO_3 according to the technique of Heinrichs & Herrmann (1990). CsCl and LiCl are added as an ionization buffer and internal standard, respectively. The analytical error for the K–Ar age

Fig. 3. (*Continued*) Width of image is *c.* 15 cm. (**b**) Microphotograph of the sandstone layer of photo (a). The texture elements are sedimentary in character, the detrital components are not oriented and deformed, the pressure solution is hardly detectable. Width of image is 4.3 mm. (**c**) Typical, crenulated texture of the low-grade metapelites. S1 and S2 are respectively the foliations developed during D1 and D2 tectonic phases according to Montomoli *et al.* (2008) and Antolin *et al.* (2011). Width of image is 3.8 mm. (**d**) In thermal aureole of the leucogranite intrusions of the Yala Xiangbo dome rutile crystals were grown in the metapelites. Width of image is 4.3 mm. (**e**) Schist-parallel and unoriented growth of millimeter sized muscovite crystals in a metamorphosed dyke. Width of image is 4.3 mm. (**f**) The typical mineral assemblage of the greenschist-facies metamorphosed dykes: chlorite > calcite ~ quartz > sphene ~ albite. Metamorphic minerals show a preferred orientation and define a coarse grain S1 foliation (Montomoli *et al.* 2008; Antolin *et al.* 2011). Width of image is 1.1 mm. (**g**) Amphibole-garnet schist (site SR-21). Width of image is 4.3 mm. (**h**) Microphotograph showing the deformation of Dala granite. The bands of biotite were formed in a partly-crystallized, semi-ductile state of granite. Width of image is 8 mm).

calculations is given on a 95% confidence level (2σ). More details of argon and potassium analyses are given in Wemmer (1991).

(U–Th)/He thermochronology

Zircon and apatite crystals were concentrated by standard mineral separation processes (crushing, sieving, gravity and magnetic separation). Only clear, intact, euhedral single crystal aliquots were dated. The shape parameters were determined and archived by multiple microphotographs and used for the correction of alpha ejection (Farley *et al.* 1996). The crystals were wrapped in *c*. 1 × 1 mm-sized platinum capsules and degassed in high vacuum by heating with an infrared diode laser. The extracted gas was purified using a SAES Ti–Zr getter at 450 °C. The chemically inert noble gases and a minor amount of other rest gases were then expanded into a Hiden triple-filter quadrupol mass spectrometer equipped with a positive ion counting detector. Crystals were checked for degassing of He by sequential reheating and He measurement. Following degassing, samples were retrieved from the gas extraction line, spiked with calibrated ^{230}Th and ^{233}U solutions. Zircons were dissolved in pressurized Teflon bombs using distilled 48% HF + 65% HNO_3 in five days at 220 °C, while apatites in 2% HNO_3. The actinide and Sm concentrations were determined by isotope dilution method using a Perkin Elmer Elan DRC II ICP-MS equipped with an APEX micro-flow nebulizer.

Results

Sheet-silicate mineralogy and Kübler Index values

The studied grain size fractions are composed mainly of illite/muscovite, chlorite, paragonite, quartz and minor albite. Kaolinite, smectite and carbonates were not detected. The illite/chlorite ratios are typically high and thus well-suited both for KI determination and for K–Ar geochronology (DB-47 in Fig. 4), but sometimes the chlorite is the dominant sheet silicate (CE-6E in Fig. 4). In some samples there is a discrepancy between the crystallinity state of illite/muscovite and chlorite, although the correlation of Kübler and Árkai indices is usually very good (e.g. Árkai 1991; Potel 2007). In these cases we assume that well-crystallized

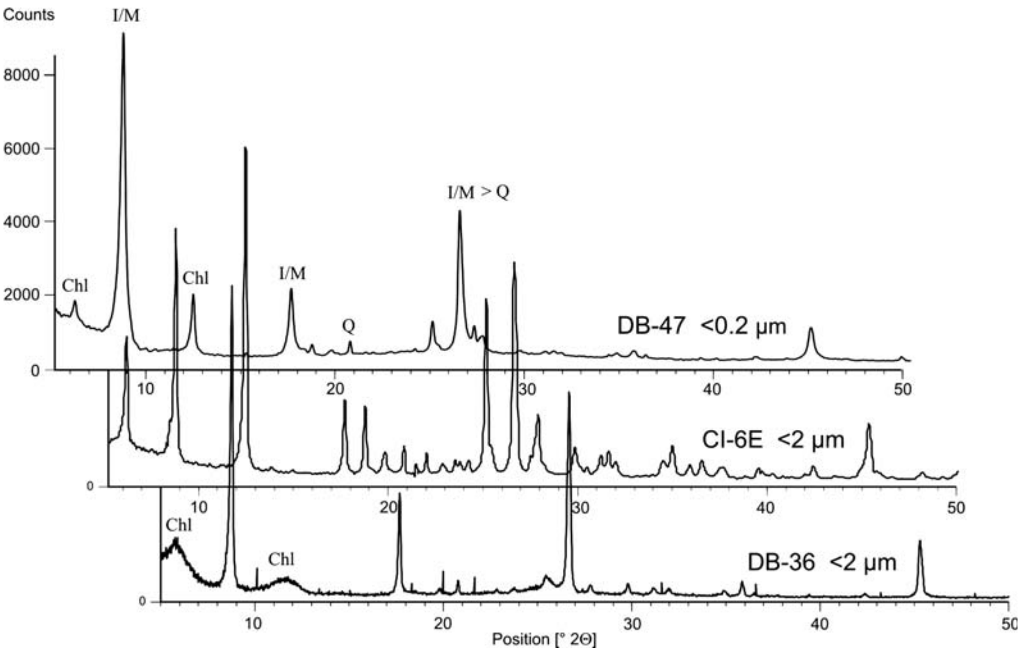

Fig. 4. XRD patterns of oriented, air-dried <2 and <0.2 µm fractions demonstrating the characteristic mineralogical composition of the analysed samples. I/M, illite/muscovite; Chl, chlorite; Q, quartz; DB-47, A typical metapelite sample, the dominant component is illite/muscovite and the amounts of Q and Chl are subordinate. CI-6E, A rare and less optimal composition, as chlorite is more abundant than illite. DB-36, Beyond the well crystallized illite the chlorite peaks are very diffuse.

illite/muscovite crystals are detrital in origin, whereas the chlorite is newly-formed at low pT conditions.

Paragonite is also present in several samples (Fig. 5a). Peak deconvolution performed on the double-peak white mica XRD patterns (using FITYK, Wojdyr 2007) suggest that K–Na 'mixed layer phases' are present (Livi *et al.* 1997; Árkai *et al.* 2003).

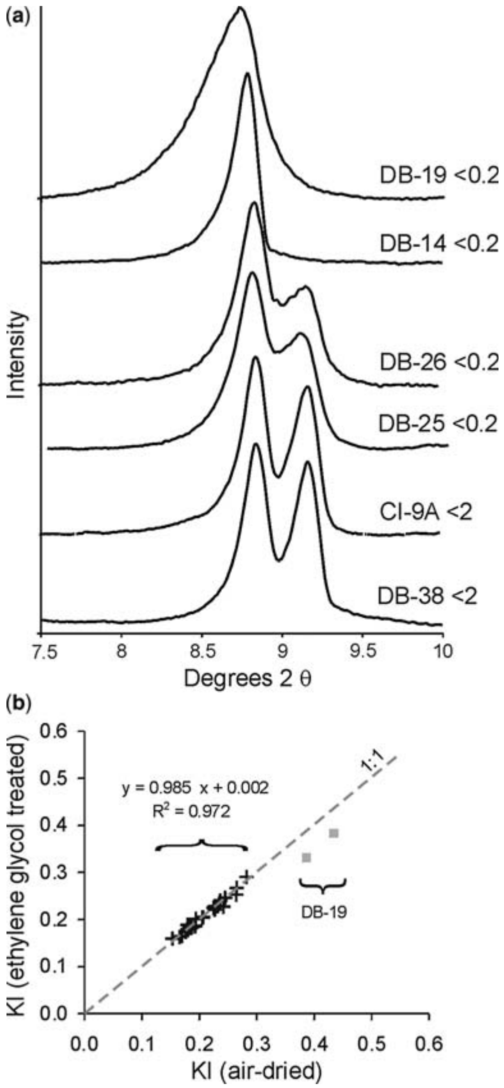

Fig. 5. (**a**) Diagnostic sections of XRD patterns showing badly and well crystallized illite (samples DB-19 and DB-14, respectively) and the paragonite-bearing samples (two peaks). (**b**) Plot of Kübler Index (KI) measured on air dried v. KI measured on ethylene glycol treated samples. For the correlation coefficient and regression parameters only the values below 0.38 were considered. The 2σ error bars of the presented values are smaller than the symbols.

The KI values dominantly indicate an anchizonal–epizonal overprint, only one sample is in the diagenetic zone (Table 1; Fig. 6a). The good correlation between the air-dried and glycolized samples indicates that there are practically no expandable smectite layers in the majority of the samples (the only exception is sample DB-19; see Fig. 5b). This property of the crystal lattice is important for the evaluation of K–Ar ages (see below).

K–Ar ages

The lack of smectite interlayers in the dated samples indicates that the proportion of exchangeable cations is low that is, crystals are closed for cation migration. Thus, we do not need to count some unpredictable Ar diffusion processes due to a non-illitic lattice.

The illite/muscovite K–Ar ages range between 106–14 Ma (see Table 2, Fig. 6b). The potassium-oxide content is in each case below the stoichiometric composition of muscovite and varies between 3.4–7.1 wt%. The proportion of radiometric argon shows an even wider scatter between 13–98%. These two parameters correlate well (Fig. 7). The samples are grouped according to the present sheet-silicate assemblage. The illite-rich samples show the highest K content and the highest proportion of radiogenic argon. The chlorite-bearing fractions contain less K and Ar*, and even smaller values are observed in the paragonite-bearing samples. Figure 7 shows high amounts of atmospheric argon in paragonite and chlorite and indicates mixing between K-bearing and K-free phases.

Vitrinite reflectance

Random vitrinite reflectance values range from 1.6–4.1%Ro. Two samples (DB-37, DB-39) contain graphitized organic matter with R_{max} values above 9.8%, Table 3). The areal distribution of the measured values in the study area is presented in Figure 6c.

Metamorphic pT conditions determined by Thermocalc and PERPLEX

Thermobarometric analyses were performed on two metamorphosed dykes collected in the NE part of the study area (WE and SR sites; see Fig. 2). The mineral paragenesis of sample WE-12 is Ms, Chl, Carb, Q, /Ep and in sample SR-21a Amp, Grt, Ep, Chl, Fsp, Q, /Carb (Fig. 3e, g). Mineralogical and textural evidences indicate the absence of a retrograde transformation or complex deformation.

Table 1. *Geographical coordinates, illite Kübler Index and K–Ar age of samples wehere beyond 'illite crystallinity' illite geochronology was also performed.*

Sample					Kübler Index		K–Ar						Ro
	Long.	Lat.	Elev.	Fraction	air dry	glyc.	<0.2 μm		<2 μm		2–6 μm		
	(°)	(°)	(m)	(μm)	(Δ°2θ)		(Ma)	±2 s	(Ma)	±2 s	(Ma)	±2 s	(%)
DB-1	89.6575	28.4848	4329	<0.2	0.193	0.187	**35.6**	1.0					
				<2	0.193	0.186			**34.6**	0.7			1.98
DB-5	90.1567	28.8988	4957	<6	0.153	0.160							1.85
DB-9	90.3183	28.8850	4637	<6	0.205								1.63
DB-14	92.2190	28.6208	5030	<0.2	0.179	0.179	**35.0**	1.1					
				<2	0.170	0.165			**37.9**	0.9			2.04
DB-19	91.6215	28.9048	4139	<0.2	0.434	0.383	**88.7**	1.5					
				<2	0.387	0.331			**106.5**	3.3			
DB-21	91.6362	28.9271	4025	<0.2	0.242	0.227	**55.7**	1.0					
				<2	0.207	0.205			**60.1**	0.8			3.77
DB-23	91.6419	28.9333	4040	<2	0.199				**61.61**	0.91			
				2–6	0.179	0.176					**73.0**	1.0	3.05
DB-25	92.1574	29.1036	3829	<0.2	***0.509***	***0.528***	**23.4**	1.9					
				<2	***0.228***	***0.229***			**32.2**	1.6			
DB-26	92.1574	29.1036	3829	<0.2	***0.232***	***0.228***	**31.6**	2.2					
				<2	***0.185***	***0.182***			**33.0**	1.5			
DB-32	91.6496	28.9522	3970	<0.2	0.227	0.221	**46.8**	1.4					
				<2	0.205	0.205			**71.8**	1.9			
DB-36	91.6764	28.9881	3858	<0.2	0.194	0.201	**32.8**	1.0					
				<2	0.166	0.163			**33.8**	0.6			
DB-38	91.6950	29.0650	3726	<0.2	***0.184***	***0.183***	**24.2**	1.2					graphite
				<2	***0.180***	***0.189***			**22.0**	1.1			
DB-44	91.3174	29.0537	3963	<0.2	0.245	0.246	**74.9**	1.2					

				<2	0.225	0.225			**82.7**	2.4			
DB-45	91.1048	29.0483	4129	<0.2	0.265	0.267	**77.8**	1.5					
				<2	0.237	0.241			**86.6**	1.1			2.76
DB-47	91.1116	29.0857	3953	<0.2	0.282	0.291	**79.0**	0.9					
				<2	0.265	0.253			**90.4**	1			
DB-55	90.6353	29.1977	4685	<0.2	0.205	0.204	**62.2**	1.3					
				<2	0.183	0.184			**63.6**	0.8			2.51
CI-6E	91.7515	29.1947	3821	<0.2	0.187	0.184	**49.0**	1.8					
				<2	0.177	0.174			**56.6**	0.8			
CI-9A	91.7045	29.0730	3693	<0.2	***0.185***		**25.7**	0.9					1.94
				<2	***0.187***				**30.0**	1.4			
DE3	92.69	28.99	10611	<2	***0.173***								
				2–6	***0.165***	0.16					**21.7**	0.4	
DE7	92.54	28.99	11493	<2	0.172	0.18							
DE8a	92.57	29.05	11015	2–6	0.160	0.17					**22.0**	0.8	
DE19	90.8410	29.28	11761	<0.2	0.171	0.17							
DR14	92.38	28.82	14584	<2	0.171	0.22			**27.6**	0.9			
				2–6	0.160	0.16					**34.4**	0.8	
DR17	9.37	28.82	14686	<2	0.153								
				2–6	0.150	0.15							
QU19	92.21	28.99	13946	<2	0.160	0.200			**48.3**	1.1			
				2–6	0.174	0.160					**51.6**	0.8	
TU6b	92.22	28.83	14913	<2	0.165				**13.9**	0.7			
				2–6	0.148	0.149					**14.2**	0.5	

Note: Italics in the columns of Kübler Index indicates that paragonite is also present among the sheet silicates. In some cases it was not possible to express the KI.

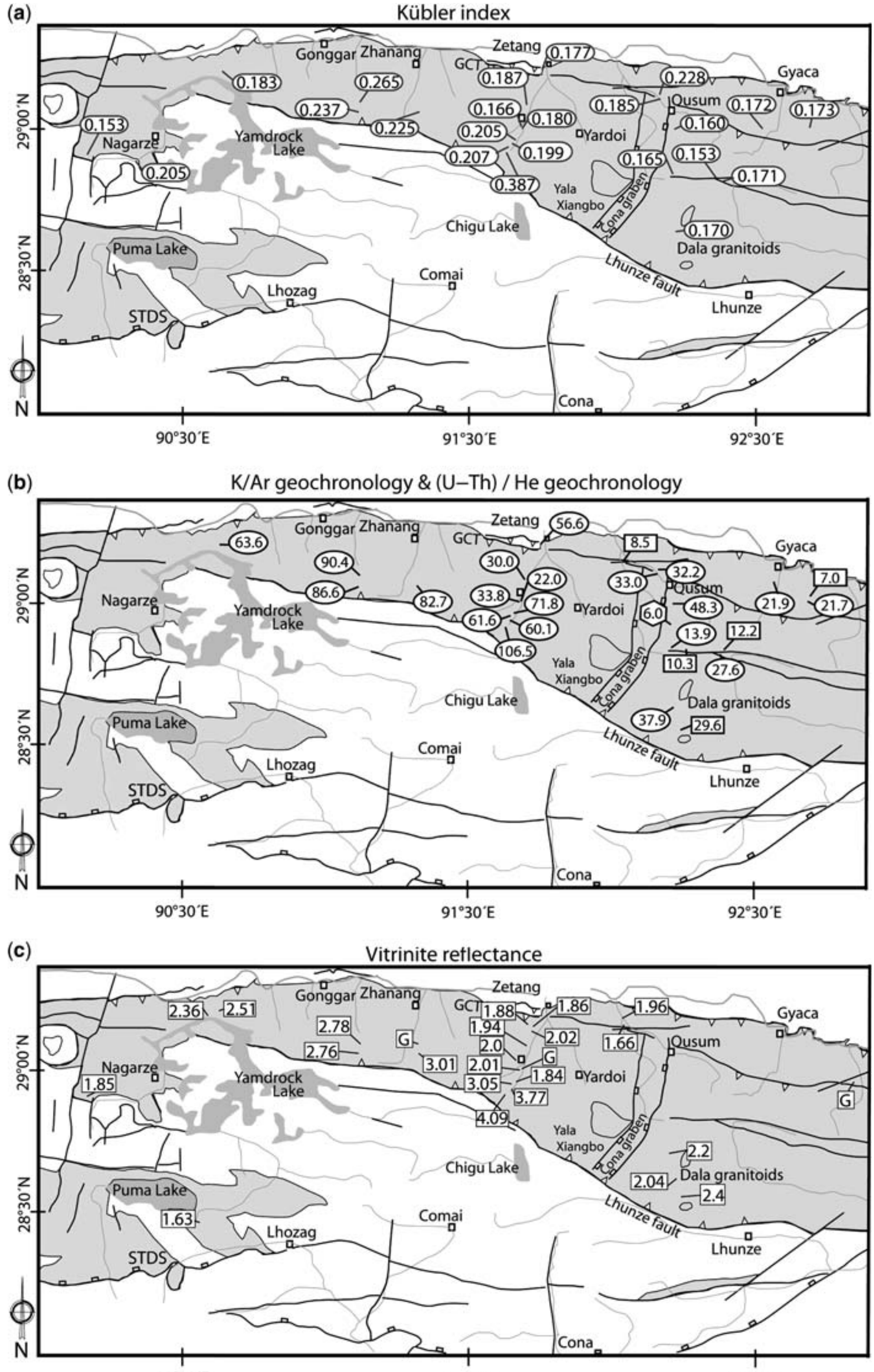

Fig. 6. Areal distribution of metamorphic and geochronological results in SE Tibet. Grey area, Triassic flysch. (**a**) Kübler Index (fraction <2 μm), (**b**) K–Ar ages of illite fractions <2 μm (in ellipses) and (U–Th)/He ages (in rectangles), (**c**) vitrinite reflectance. G: graphite particles recorded in the organic matter. Uncertainties of the plotted values and analytical details are in Tables 1–5.

Table 2. *K–Ar ages of illite fractions of fine grained (meta)pelitic members of Tethyan flysch and of coarse muscovites formed in metabasic rocks*

Sample	Fraction (μm)	K_2O (wt. %)	$^{40}Ar^*$ ([nl/g]) STP	$^{40}Ar^*$ (%)	Age (Ma)	2 s-Error (Ma)
Illite-rich fractions from (meta)pelitic samples from the Tethyan flysch						
DB-1	<2	4.93	5.56	50.3	**34.6**	0.7
DB-1	<0.2	4.81	5.57	54.3	**35.6**	1.0
DB-14	<2	7.11	8.79	54.7	**37.9**	0.9
DB-14	<0.2	6.75	7.69	47.0	**35.0**	1.1
DB-19	<2	6.09	21.56	94.4	**106.5**	3.3
DB-19	<0.2	6.47	18.98	94.0	**88.7**	1.5
DB-21	<2	6.44	12.70	87.6	**60.1**	0.8
DB-21	<0.2	6.32	11.53	86.5	**55.7**	1.0
DB23	<2	5.17	10.45	83.9	**61.6**	0.9
DB23	2–6	4.18	10.04	76.3	**73.0**	1.0
DB-25	<2	3.44	3.61	19.6	**32.2**	1.6
DB-25	<0.2	3.63	2.76	12.9	**23.4**	1.9
DB-26	<2	3.65	3.92	23.1	**33.0**	1.5
DB-26	<0.2	3.58	3.67	21.8	**31.6**	2.2
DB-32	<2	3.81	9.00	79.5	**71.8**	1.9
DB-32	<0.2	5.61	8.58	72.9	**46.8**	1.4
DB-36	<2	6.49	7.15	56.0	**33.8**	0.6
DB-36	<0.2	6.07	6.48	52.0	**32.8**	1.0
DB-38	<2	5.24	3.74	31.0	**22.0**	1.1
DB-38	<0.2	4.34	3.40	27.7	**24.2**	1.2
DB-44	<2	5.32	14.53	89.0	**82.7**	2.4
DB-44	<0.2	5.42	13.36	85.1	**74.9**	1.2
DB-45	<2	5.51	15.76	91.7	**86.6**	1.1
DB-45	<0.2	5.67	14.55	90.4	**77.8**	1.5
DB-47	<2	5.65	16.90	90.6	**90.4**	1.0
DB-47	<0.2	6.08	15.82	88.5	**79.0**	0.9
DB-55	<2	6.05	12.63	82.1	**63.6**	0.8
DB-55	<0.2	5.92	12.07	82.5	**62.2**	1.3
CI-6E	<2	4.83	8.96	82.8	**56.6**	0.8
CI-6E	<0.2	4.89	7.83	71.2	**49.0**	1.8
CI-9A	<2	4.27	4.17	45.7	**30.0**	1.4
CI-9A	<0.2	4.56	3.80	42.7	**25.7**	0.9
DE3	2–6	6.52	4.60	76.7	**21.7**	0.4
DE8a	2–6	2.91	2.07	30.1	**22.0**	0.8
DR14	<2	5.92	5.31	33.2	**27.6**	0.9
DR14	2–6	5.15	5.77	45.4	**34.4**	0.8
QU19	<2	6.04	9.53	44.7	**48.3**	1.1
QU19	2–6	5.14	8.67	64.3	**51.6**	0.8
TU6b	<2	5.24	2.36	19.1	**13.9**	0.7
TU6b	2–6	3.86	1.77	28.4	**14.2**	0.5
Coarse muscovite of the greenschist (meta-basalt)						
WE-12	125–250	7.57	10.90	96.8	**44.1**	0.5
WE-10A	125–250	8.52	12.16	98.4	**43.7**	0.6

Site WE-12. For Thermocalc method 19 analyses of a total of 74 spots were selected. Table 4 shows the averages of the selected analyses for the Thermocalc computations as well as the cations per formula unit. The calculations of the cations per formula unit were done with AX. For the calculations the CO_2-fraction of the fluid-phase was set to 10%. The obtained pT results for sample WE-12 are $T = 474 \pm 35$ °C & $P = 6.4 \pm 1.6$ kbar ($\sigma_{fit} = 1.64$). Even though Thermocalc estimates a 2σ temperature error of 35 °C (output), because of various methodological error sources (Kohn & Spear 1991; Powell & Holland 1994), it should be replaced by a minimum error of 50 °C (Powell & Holland 2008).

Site SR-21a. Thermocalc evaluations of sample SR-21-a were performed on mineral assemblages in the vicinity of garnets. According to microstructural

Table 3. *Vitrinite reflectance values measured on (meta)pelitic samples of SE Tibet*

Sample	Long. (°)	Lat. (°)	Elev. (m)	Ro (%)	sd	R_{max} (%)	sd	R_{min} (%)	sd	N
DB-1	89.6575	28.4848	4329	**1.98**	0.27					50
DB-3	89.6640	28.4967	4341	**2.01**	0.29					22
DB-5	90.1567	28.8988	4957	**1.85**	0.30					19
DB-10	90.5334	28.4597	5128	**1.63**	0.16					24
DB-13	92.2446	28.5411	4373	**2.40**	0.19					39
DB-15	92.2190	28.6208	5030	**2.04**	0.33					14
DB-16	92.1906	28.7015	4844	**2.20**	0.26					16
DB-19	91.6215	28.9048	4139	**4.09**	0.24					30
DB-21	91.6362	28.9271	4025	**3.77**	0.21					30
DB-23	91.6419	28.9333	4040	**3.05**	0.31					50
DB-28	92.0433	29.1454		**1.66**	0.27					22
DB-30	92.0321	29.1714	3614	**1.96**	0.25					19
DB-32	91.6496	28.9522	3970	**1.84**	0.24					6
DB-33	91.6564	28.9649	3939	**2.01**	0.30					5
DB-42	91.3024	29.0303	4092	**3.01**	1.59					8
DB-45	91.1048	29.0483	4129	**2.76**	0.36					50
DB-47	91.1116	29.0857	3953	**2.78**	0.28					50
DB-54	90.5926	29.1888	4502	**2.36**	0.26					50
DB-55	90.6353	29.1977	4685	**2.51**	0.22					50
CI-9B	91.7045	29.0730	3693	**1.94**	0.21					22
CI-17M	91.7210	29.1487	3634	**1.86**	0.25					30
CI-15B	91.7107	29.1275	3648	**2.02**	0.18					5
DE-16C	91.7210	29.1487	3634	**1.88**	0.21					30
DE-17B	91.6671	29.0150	3846	**2.00**	0.21					30
Graphite-bearing samples										
DB-37	91.6794	29.0099	3812			10.4	0.98	1.19	0.38	26
DB-39	91.3100	29.0874	3655			9.85	0.84	1.43	0.73	18
DB-39	91.3100	29.0874	3655	graphite particles						
SR-21a	92.86	28.95	3389	graphite						

observations, the Grt–Fsp–Chl–Am assemblage is in equilibrium. In the surroundings of eight selected garnet crystals a total of 122 spot analyses were performed in the adjacent mineral phases. Analyses of the garnet rims were used to estimate the metamorphic conditions with Thermocalc (Spear 1995). The garnet compositions determined in the cores of the crystals forms the base for the PERPLEX method. The results of two data sets yielding the smallest 2σ errors (see Table 4) are 531 °C (2σ = 13 °C), 9.4 kbar (2σ = 1.0 kbar) at $\sigma_{fit} = 0.87$ and 511 °C (2σ = 12 °C), 10.0 kbar, (2σ = 0.9 kbar) at $\sigma_{fit} = 0.48$, respectively.

The reported 2s errors are underestimating the real uncertainty (see above), thus we use a minimum of 50 °C and 1 kbar respectively.

For the PERPLEX calculations 10 spot analyses of garnet cores, with totals between 99.5 wt% and 101 wt%, were selected and averaged (Table 4). The PERPLEX garnet isopleths for sample SR-21-a are depicted in Figure 8. The pT result for this sample is estimated by 600 ± 50 °C and 7.4 ± 1.5 kbar.

(U–Th)/He ages

Zircon and apatite helium ages (ZHe and AHe, respectively) together with the analytical details are listed in Table 5. The dated localities are plotted in Figure 6b. The amounts of actinide elements for all single crystal ZHe measurements are at least 20 times higher than the limit of detection. The ZHe ages are slightly different in the samples, but they cluster mainly in the Late Miocene (12.2–7 Ma), only the southernmost sample (DB-12) resulted in an Oligocene age. Only one sample of a metamorphosed dyke (WE-12) contains proper apatite crystals for He-chronology resulting in a Late Miocene AHe age.

Discussion

Low-grade pelites potentially contain detrital white mica grains, carrying the signal of the crystallization conditions and age of the source region of the sediment (Hower *et al.* 1963; Hurley *et al.* 1963). The

Table 4. *Average chemical and cation composition of the mineral phases used for thermobarometry. Oxygen numbers used for cation numbers are: MS: 11, Chl: 14, Carb: 6, Ep: 12.5, Grt: 12, Fsp:8 Amph: 23*

WE-12 greenschist

Mineral	**SiO_2**	**TiO_2**	**Al_2O_3**	**Cr_2O_3**	**Fe_2O_3**	**FeO**	**MnO**	**MgO**	**CaO**	**Na_2O**	**K_2O**
Ms	46.33	0.17	35.44	0.00	0.00	1.04	0.01	0.73	0.03	1.09	9.01
Chl	24.61	0.04	23.47	0.08	0.00	26.18	0.31	13.12	0.01	0.01	0.01
Carb	0.02	0.01	0.01	0.01	0.00	1.23	0.75	0.56	59.04	0.01	0.02
Ep	38.49	0.08	25.29	0.01	10.08	0.61	0.03	0.01	23.70	0.00	0.01
Mineral	**Si**	**Ti**	**Al**	**Cr**	**Fe3**	**Fe2**	**Mn**	**Mg**	**Ca**	**Na**	**K**
Ms	3.10	0.01	2.80	0.00	0.00	0.06	0.00	0.07	0.00	0.14	0.77
Chl	2.60	0.00	2.92	0.01	0.00	2.31	0.03	2.06	0.00	0.00	0.00
Carb	0.00	0.00	0.00	0.00	0.00	0.03	0.02	0.03	1.92	0.00	0.00
Ep	3.02	0.01	2.34	0.00	0.60	0.04	0.00	0.00	1.99	0.00	0.00

SR-21a amphibole-garnet schist: compositios used for Thermocalc

Assemblage #1	**SiO_2**	**TiO_2**	**Al_2O_3**	**Cr_2O_3**	**Fe_2O_3**	**FeO**	**MnO**	**MgO**	**CaO**	**Na_2O**	**K_2O**
Grt	38.15	0.10	20.97	0.00	0.00	27.01	2.93	1.72	9.79	0.02	0.00
Fsp	66.34	0.00	21.32	0.00	0.27	0.00	0.03	0.00	2.10	10.50	0.03
Chl	25.66	0.06	19.93	0.07	0.27	28.94	0.44	12.65	0.03	0.00	0.01
Am	45.08	0.42	14.31	0.03	0.27	17.14	0.24	8.73	9.66	2.43	0.11
Assemblage #2											
Grt	37.58	0.09	20.46	0.03	0.10	27.09	3.13	1.77	8.97	0.02	0.00
Fsp	68.31	0.00	19.75	0.01	0.00	0.00	0.00	0.00	0.24	11.67	0.04
Chl	24.85	0.04	18.83	0.00	0.00	28.40	0.42	12.86	0.02	0.01	0.01
Am	45.63	0.32	11.51	0.04	3.30	12.87	0.17	10.38	10.01	2.02	0.14
Assemblage #1	**Si**	**Ti**	**Al**	**Cr**	**Fe^3**	**Fe^2**	**Mn**	**Mg**	**Ca**	**Na**	**K**
Grt	3.02	0.01	1.96	0.00	0.00	1.79	0.20	0.20	0.83	0.00	0.00
Fsp	2.90	0.00	1.10	0.00	0.01	0.00	0.00	0.00	0.10	0.89	0.00
Chl	2.75	0.01	2.52	0.01	0.02	2.60	0.04	2.02	0.00	0.00	0.00
Am	6.61	0.05	2.48	0.00	0.03	2.10	0.03	1.91	1.52	0.69	0.02
Assemblage #2											
Grt	3.02	0.01	1.94	0.00	0.01	1.82	0.21	0.21	0.77	0.00	0.00
Fsp	2.98	0.00	1.02	0.00	0.00	0.01	0.00	0.00	0.01	0.99	0.00
Chl	2.75	0.00	2.46	0.00	0.00	2.63	0.04	2.12	0.00	0.00	0.00
Am	6.77	0.04	2.01	0.01	0.37	1.60	0.02	2.30	1.59	0.58	0.03

SR-21a amphibole-garnet schist: average garnet core composition used for PERPLEX

Mineral	**SiO_2**	**TiO_2**	**Al_2O_3**	**Cr_2O_3**	**Fe_2O_3**	**FeO**	**MnO**	**MgO**	**CaO**	**Na_2O**	**K_2O**
Grt	37.90	0.13	20.56	0.03	0.15	26.90	3.96	1.65	9.14	0.00	0.00
Mineral	**Si**	**Ti**	**Al**	**Cr**	**Fe^3**	**Fe^2**	**Mn**	**Mg**	**Ca**	**Na**	**K**
Grt	3.02	0.01	1.93	0.00	0.01	1.79	0.27	0.20	0.78	0.00	0.00

Table 5. *Results of (U–Th)/He geochronology*

Sample	aliq.	He		U238		Th232		Sm			Ejection	*Uncorr.*	Ft-Corr.		Sample unweighted aver. (1 s.e.)	
		vol. (ncc)	s.e. (ncc)	mass (ng)	s.e. (ng)	Mass (ng)	s.e. (ng)	Th–U Ratio	Mass (ng)	s.e. (ng)	correct. (Ft)	*He-age (Ma)*	*He-age* (Ma)	1 s (Ma)		
Zircon																
DB-27 *(3865 m)*	#1	2.661	0.045	3.048	0.055	1.195	0.029	0.39	0.028	0.002	0.70	*6.6*	**9.5**	0.2		
	#2	0.981	0.017	1.125	0.020	0.538	0.013	0.48	0.052	0.003	0.76	*6.5*	**8.5**	0.2		
	#3	0.781	0.014	0.890	0.016	0.718	0.017	0.81	0.065	0.004	0.80	*6.1*	**7.6**	0.2	**8.5**	**0.5**
DR13 *(4523 m)*	#1	2.591	0.044	2.048	0.037	0.765	0.018	0.37	0.031	0.002	0.78	*9.6*	**12.4**	0.3		
	#2	5.782	0.096	4.092	0.074	2.234	0.054	0.55	0.052	0.003	0.80	*10.4*	**13.0**	0.3		
	#3	2.193	0.037	1.945	0.035	0.406	0.010	0.21	0.028	0.002	0.79	*8.9*	**11.2**	0.3	**12.2**	**0.5**
MV31c *(3440 m)*	#1	0.633	0.012	1.043	0.019	0.196	0.005	0.19	0.004	0.000	0.74	*4.8*	**6.5**	0.2		
	#2	1.582	0.027	2.234	0.040	0.523	0.013	0.23	0.016	0.004	0.73	*5.6*	**7.6**	0.2	**7.0**	**0.5**
TU-4a *(4655 m)*	#1	5.245	0.087	5.136	0.093	1.873	0.045	0.36	0.069	0.002	0.77	*7.8*	**10.1**	0.2		
	#2	1.934	0.033	1.804	0.033	1.013	0.024	0.56	0.040	0.002	0.78	*7.8*	**10.0**	0.2		
	#3	1.749	0.029	1.643	0.030	0.869	0.021	0.53	0.021	0.001	0.74	*7.8*	**10.6**	0.2		
	#4	1.268	0.022	1.242	0.023	0.465	0.011	0.37	0.022	0.001	0.74	*7.8*	**10.5**	0.2	**10.3**	**0.1**
DB-12 *(4373 m)*	#1	4.431	0.073	1.564	0.028	0.764	0.018	0.49	0.032	0.002	0.68	*21.0*	**30.7**	0.7		
	#2	2.151	0.036	0.735	0.013	0.627	0.015	0.85	0.019	0.001	0.69	*20.1*	**29.3**	0.7		
	#3	2.227	0.037	0.716	0.013	0.770	0.019	1.08	0.016	0.001	0.71	*20.5*	**28.9**	0.6	**29.6**	**0.5**
Apatite																
WE-12 *(4437 m)*	#1	0.001	0.000	0.001	0.001	0.004	0.000	7.52	0.119	0.011	0.78	*4.4*	**5.6**	1.9		
	#2	0.001	0.000	0.001	0.001	0.005	0.000	5.33	0.160	0.015	0.67	*3.8*	**5.6**	1.5		
	#3	0.008	0.001	0.005	0.001	0.018	0.001	3.86	0.553	0.050	0.71	*4.6*	**6.4**	0.6		
	#4	0.011	0.001	0.007	0.000	0.029	0.001	4.47	0.846	0.077	0.76	*4.4*	**5.8**	0.4		
	#5	0.026	0.001	0.013	0.001	0.066	0.002	4.99	1.752	0.158	0.76	*5.0*	**6.6**	0.4	**6.0**	**0.2**

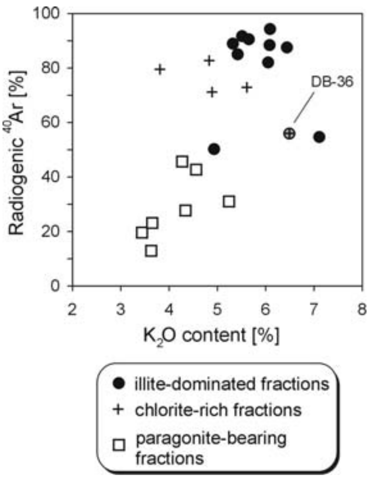

Fig. 7. Plot of potassium content v. the proportion of radiogenic argon and the mineralogy of the dated sheet-silicate rich fractions. The 2σ error bars of the presented values are smaller than the symbols. The DB-36 sample contains the badly crystallized chlorite (see Fig. 4).

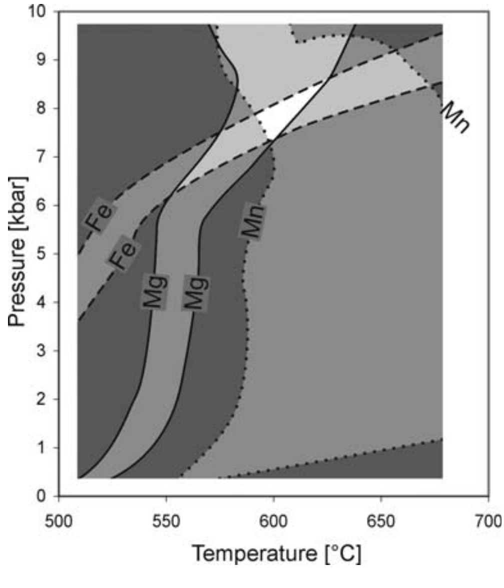

Fig. 8. Metamorphic pressure and temperature conditions (white area) of amphibole-garnet schist of SR 21 site determined by PERPLEX method. Paired garnet isopleths demarcate the stability field of garnet that is in equilibrium with the bulk rock chemistry and mineral paragenesis. The lines show the ± 1 s.d. of the chemical compositions determined in the cores of the garnet crystals by multiple electron microprobe analyses (see Table 4).

distinction of the inherited and newly formed generations of sheet silicates in grain size fractions is difficult and such aliquots result in typically mixed ages. However, white micas formed in basic and intermediate magmatic rocks are exclusively metamorphic in origin. Therefore these white micas are free of any inherited signals and their K–Ar ages reflect the age of metamorphism or cooling. Thus, we will separately discuss the results yielded from metapelitic and metabasic lithologies.

Conditions and age of metamorphism of some basic dykes

Thermobarometric analyses indicate greenschist facies metamorphism for the WE sites and amphibolite facies metamorphism for the SR sites.

The greenschists of the WE sites contain well developed white mica crystals (Fig. 3e). They are aligned along the main foliation, indicating crystallization during the S1 tectonic phase (Montomoli *et al.* 2008; Antolin *et al.* 2011). White mica does not occur in mafic magmatic rocks as primary phase and the texture of this folded greenschist does not show any relict magmatic element. Therefore, the muscovites are completely metamorphic in origin. In these sites S2 foliation is a crenulation cleavage not associated to dynamic recrystallization (Antolin *et al.* 2011). The corresponding K–Ar ages are 43.7 and 44.1 Ma. Noticeable are the high percentages of radiogenic argon (Table 2). The two samples were collected in *c.* 1 km distance from two distinct metamagmatite bodies of different chemistry and deformation degree. We interpret these ages as the formation age of the muscovites, recording the age of greenschist facies metamorphism that took place in a part of the THS east of the Yala Xiangbo dome. These ages resemble the emplacement age of the Dala granite (44.1 $\pm$ 1.2 Ma, U–Pb zircon dating; Aikman *et al.* 2008), located 25 km SE of the sampled sites. At this location the Dala granite intruded into a low structural level and experienced some near-solidus deformation (Fig. 3h) that occurred simultaneously or soon after the emplacement. Similar ages (*c.* 44 Ma) for peak metamorphic conditions have been detected also in the underlying GHS tectonic unit using Th–Pb and U–Pb datings on monazites (Catlos *et al.* 2002, 2007; Carosi *et al.* 2010).

The key observation for the amphibole-garnet schist of SR site is the difference in the calculated pressures using Thermocalc and PERPLEX methods. The Thermocalc p-estimate of the garnet rim assemblages is at least 2 kbar higher than the PERPLEX estimate of the garnet core. This indicates prograde metamorphism during garnet growth.

Here it is important to note that the studied site is far away (>60 km) from the next metamorphic dome (Yala Xiangbo dome). Thus an immediate heating from the lower structural unit has to be excluded. The available samples did not allow geochronological dating, but we assume that the amphibolite facies metamorphism was co-genetic with the *c*. 44 Ma old greenschist facies event detected at the WE sites, discussed above.

Low-grade metamorphism of metapelitic samples

The geothermometrical and geochronological data from sub-greenschist facies pelitic lithologies are not so well constrained as the results measured on orthometamorphic rocks of higher pT conditions (like the data discussed above). Anchi- and epizonal conditions result in incomplete, disequilibrium phase transformations. This fact is supported by field observations. The metapelitic samples show a very variable intensity of white-mica growth, even detectable within a single outcrop. The mica growth process is strongly controlled by the host lithology. In silty and sandy protoliths the neoformation of white mica is in a more advanced state than in neighbouring pelitic lithologies. We assume that three major factors are responsible for this difference: (1) the high permeability of the arenitic lithologies; (2) the local liberation of potassium and increase of K^+ activity during decomposition of feldspar grains and lithic fragments in arenites; and (3) the presence of dispersed organic material in pelitic lithologies probably embedding the silicate phases and reducing locally the diffusivity and mineral growth.

Figure 6 presents the results obtained on metapelitic samples projected on the schematic geological map of the study area. The sample sites with the highest metamorphic degree are related to tectonic slices derived from the deeper part of the THS situated close to the Yala Xiangbo dome (e.g. site TU-6). For the proper understanding of the evolution of the studied THS area we have to evaluate the KI data in concert with the argon geochronology. In epi- and anchizonal overprinted areas the mineral transformation is usually incomplete and the individual crystallinity and age data typically show apparent values, which are actually points along mixing or transformation curves. The interpretation of individual data is difficult and can result in misleading conclusions. Thus, we do not force an individual interpretation for each single sample or sample site, but rather to process all data synoptically in order to identify the major epochs of the thermal evolution for the entire eastern THS.

The KI values are controlled by the ratio of newly formed to detrital illite. It usually increases towards finer size fractions. Using two fractions, the finer one is richer in newly formed sheet silicates and always indicates a value closer to the conditions of the latest metamorphic event (Reuter 1987; Clauer & Chaudhuri 1999). The same is true for the K–Ar ages of these size fractions. The detrital grains carry an old age signal, while the newly grown population gives always a younger K–Ar age (Hower *et al.* 1963; Hurley *et al.* 1963). By combining the KI with the K–Ar ages, the ratio of newly formed to detrital illite can be estimated, especially if the initial detrital age is known.

The KI measured on different size fractions and the corresponding K–Ar ages of the metapelites in SE Tibet are plotted on Figure 9. The plot shows clear trends. The older K–Ar ages are measured in samples having a lower KI. With increasing KI the argon ages are getting younger. The <0.2 µm fractions, being rich in newly formed illite, show less ordered illite structures and younger K–Ar ages than the <2 µm fractions. The distances between the projection points of the two size fractions become smaller with increasing metamorphic degree. For samples showing the youngest K–Ar ages, the two fractions give indistinguishable results. We assume that in these cases both size fractions are dominated by the newly formed white mica. This convergence indicates equilibrium conditions and the ages (*c*. 24–22 Ma) are considered as the cessation of illite growth. These sites are structurally controlled by the D2 deformation and S2 foliation became the main penetrative foliation (Harrison *et al.* 2000; Montomoli *et al.* 2008; Antolin *et al.* 2011).

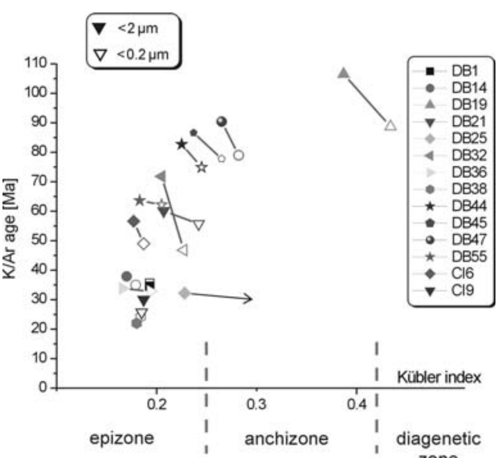

Fig. 9. Plot of Kübler Index v. K–Ar age measured on the same fraction. Note that <0.2 µm fractions show smaller degree of illite crystallinity and younger K–Ar age compared to <2 µm fractions.

For this reason the new growth of illite at *c*. 24–22 Ma is most likely related to the development of the S2 foliation.

Estimation of the maximum metamorphic temperature of metapelites by organic maturation

The vitrinite reflectance cannot be converted directly to temperature, because the transformation of organic material is a kinetic process (e.g. Barker & Pawlewicz 1986; Sweeney & Burnham 1990). Peak temperature estimation for the Triassic flysch was performed by means of three different algorithms, assuming different effective heating times (Fig. 10). For the selection of the most reliable curve we have to consider the effective heating time. The above outlined K–Ar ages indicate that the final metamorphism of the Triassic flysch took place in Oligocene–Miocene time, thus we exclude both long-lasting maximum temperature conditions as well as a shock-heating process. The most probable duration of the maximum temperature is between *c*. 5 and 15 Ma. Thus, we use the Bostick (1979) and the Sweeney & Burnham (1990) algorithms assuming 10 Ma effective heating time to estimate the range of maximum temperature (Fig. 10). Considering this conversion, the lowest vitrinite reflectance values (around Ro = 1.65%) indicate *c*. 170–185 °C maximum temperature. Typical reflectance values around 2–3%Ro indicate *c*. 180–200 and 225–235 °C maximum temperatures, respectively. Above *c*. 4% reflectance the transformation of Ro values to temperature is not properly calibrated (see e.g. Judik *et al.* 2008), thus for the estimation of maximum metamorphic temperature of the Triassic flysch we have to use the inorganic mineral phases of the metamorphosed dikes of the sequence (see above).

Miocene greenschist facies metamorphism at the base of THS

The sample set of site TU-6 was collected close to the detachment of the Yala Xiangbo dome, a zone that was intruded by thin leucogranitic and aplitic dykes. The dykes have only weekly developed chilled margins. This sample site represents a deep structural level of the THS. Newly grown, well developed muscovite crystals dominate the microtexture and KI indicates a highly crystalline lattice of the white mica. The muscovite K–Ar ages are the youngest in the studied sample set (14.2–13.9 Ma; Fig. 6b). This age range is close to the *c*. 13.5 Ma muscovite K–Ar age reported from the Yala Xiangbo dome by Aikman *et al.* (2004).

Post-sedimentary metamorphic evolution of the Tethyan flysch in SE Tibet

The evolution of the region is rather complex. To better describe the evolution of the eastern

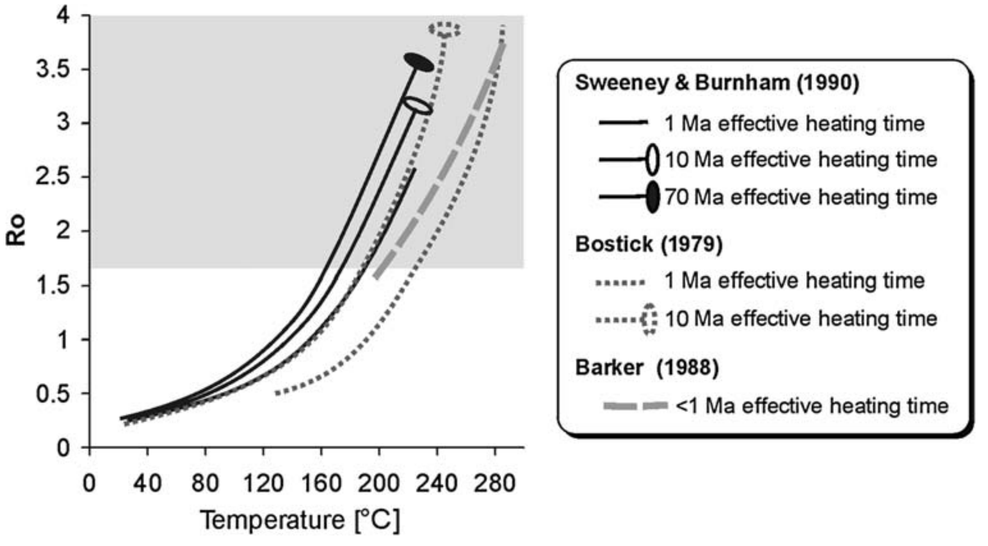

Fig. 10. Estimation of palaeotemperature from vitrinite reflectance values. Three different algorithms were used for conversion assuming different effective heating times. Grey belt represents the vitrinite reflectance values (except the graphitized samples). Evaluation is in the text.

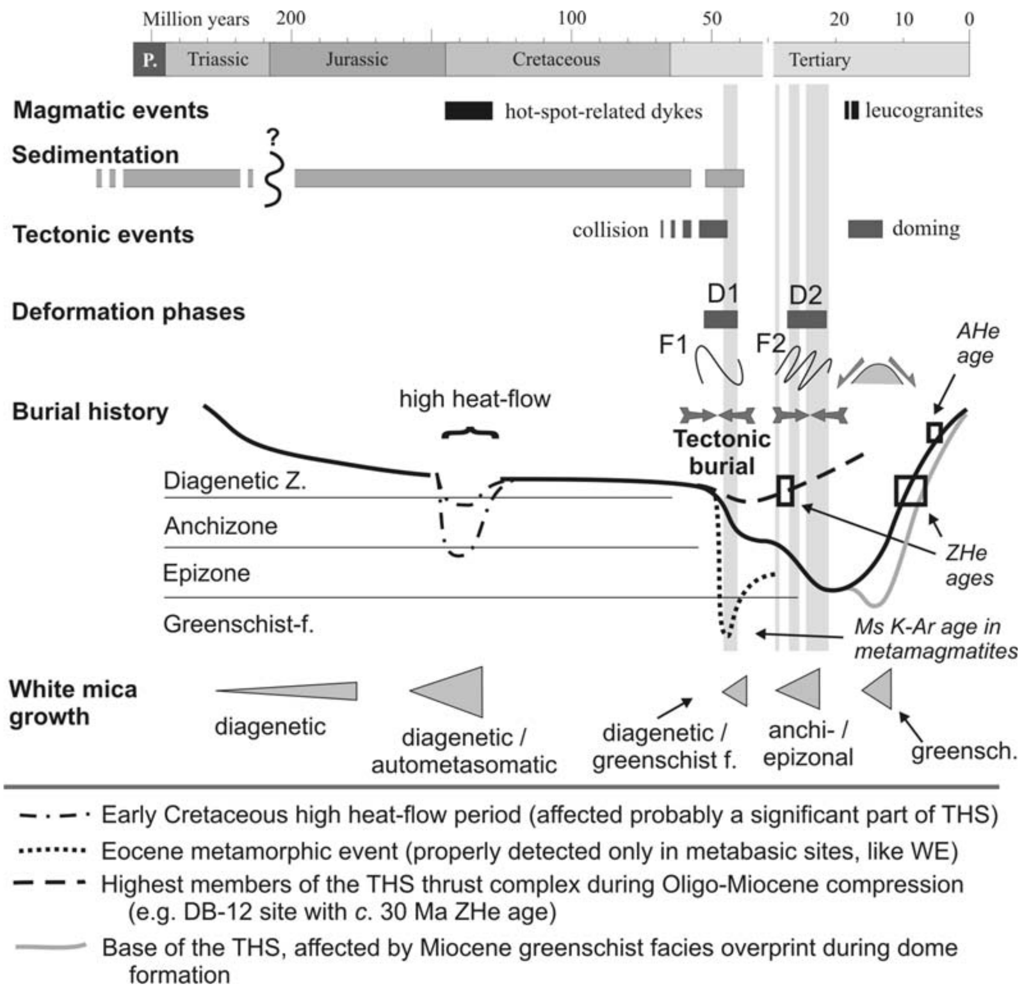

Fig. 11. Synopsis of the tectonothermal evolution of the Tethyan Himalayan flysch in SE Tibet. Time intervals emphasized by grey vertical lines are the major deformation periods dated as *c*. 44 Ma and an Oligo-Miocene one, which terminated at *c*. 24–22 Ma. Different processes were resulted in white mica growth, which took place in more periods, both in diagenetic and in metamorphic conditions. Lines represent the evolutions of different tectonic blocks of THS.

Tethyan Himalayan Sequence we compiled therefore the known thermal and tectonic events and the assumed mineral transformations and illite forming periods in a scheme (Fig. 11).

The burial history is reconstructed from the subsidence curve of Jadoul *et al.* (1998) estimating the minimum amount of burial of the Triassic flysch. In their study the sedimentary sequence was interpreted as a near-shore facies assemblage, thus, according to the observed facies differences, the thickness of the total Mesozoic pile in the study area is probably much higher. In the assumed depth of at least 4 to 5 km, the burial diagenesis can already generate new clay mineral assemblages (Meunier & Velde 2004), thus we consider the sedimentary burial as the first illite-forming epoch (Fig. 11).

The oldest argon ages of the coarsest size fractions, dominated by detrital mica, are much younger than the typical Precambrian mica ages of the Indian basement rock, being presumably the source area of the flysch (Gaetani & Garzanti 1991). They are even younger than the *c*. 250–210 Ma age of sedimentation. On the other hand, the oldest detrital (mixed) ages are older than the Eocene (*c*. 44 Ma) greenschist facies metamorphic event detected in the metabasic rocks. The lack of pre-Mid Cretaceous detrital mica ages indicates that there was a post-sedimentary reset older than the Cenozoic collision of THS. The most plausible candidate for the post-Triassic, pre-Eocene thermal reset of the detrital mica Ar-age is the high heat flow during Early Cretaceous magmatism of the region (Zhu *et al.* 2008; Xu *et al.* 2009). We assume that at *c*. 140 Ma a significant part of the THS was in anchi- and epizonal conditions and the emplacement of the dykes and the formation of their hydrothermal aureoles triggered the formation of white mica in the pelites (Fig. 11).

During Eocene times the THS experienced locally greenschist and probably also amphibolite facies metamorphism. This metamorphic event was related to the underthrusting of tectonic units during the Himalayan collision. A part of our data measured on metapelites shows a very weak overprint, thus several tectonic blocks-mainly in the southern part of the THS-occupied only shallow depths during the Eocene subduction.

During Oligo-Miocene times the ongoing shortening deformed the northern zones of the THS (Harrison *et al.* 2000; Montomoli *et al.* 2008; Antolin *et al.* 2011). The formation of illite is common, but the intensity of the deformation and the mineral growth is very variable (Fig. 11). The majority of the KI and K–Ar data from the THS were formed in disequilibrium conditions and actually they are the results of pre-Neogene and Neogene events (see e.g. Fig. 9). This indicates that the maximum thermal overprint during Miocene times usually did not exceed anchizonal–epizonal conditions. After the Oligocene to Miocene stacking, the pile of the Tethyan Himalaya was penetrated by the Yala Xiangbo dome and associated leucogranitic dykes (TU-6 site) reached greenschist facies conditions. The youngest K–Ar ages are around 14 Ma and they were measured on samples from the deepest part of the sequence, probably close to the basal detachment (represented by gray line in Fig. 11). However, this overprint was local, because in the main part of the THS the illite K–Ar ages typically show only partial reset and the newly grown illite has a low degree of crystallinity.

The obtained ZHe ages (between 30 and 7 Ma) are interpreted as cooling ages. Samples from the northern part of THS indicate a complete reset in the Miocene and prove that the currently exposed level of the THS was situated deeper than the *c*. 180 °C isotherm until the Late Miocene. The oldest ZHe age (sample DB-12: 39.6 Ma) was measured on a site at the southern margin of the Triassic flysch belt, which experienced only a diagenetic overprint. This Oligocene He-age and the weak overprint indicate that some tectonic blocks in the southern part of the flysch belt were in a shallow position, both during Eocene subduction and during Oligo-Miocene shortening (represented by dashed line in Fig. 11).

The only sample that contains datable apatite crystals yields a 6 Ma AHe age. This single datum and the calculated *c*. 70 °C closure temperature suggest an average post-Miocene cooling rate of *c*. 10 °C/Ma.

Conclusions

- The different tectonic blocks of the THS in SE Tibet experienced a thermal overprint between *c*. 170–600 °C.
- The Tethyan Triassic flysch sequence registers four tectonothermal events.
  (1) *Early Cretaceous.* Due to the subsequent events its direct dating is not possible. Nevertheless from the hot-spot related magmatism penetrating the region and from the missing pre-Mid Cretaceous illite/muscovite argon ages, we assume an Early Cretaceous period of high heat flow resulting in the formation of illite in the metapelites.
  (2) *Eocene (*c*. 44 Ma).* The early Himalayan granites (Dala granitoids; Aikman *et al.* 2008) intruded during or slightly before the greenschist and locally probably even amphibolite facies metamorphism. Maximum temperature and pressure conditions of *c*. 600 °C and 7.8 kbar indicate that a part of the THS was subducted to mid-crustal levels. This metamorphic event is probably contemporaneous with the collision related deformation phase (e.g. Godin 2003; Carosi *et al.* 2007) or Eohimalayan phase (Hodges 2000; Guillot *et al.* 2003).
  (3) *Oligo-Miocene (terminated at* c. *22 Ma).* The northern part of the THS, from Zetang to the east, experienced anchi- to epizonal metamorphism with a of deformation and thermal alteration. We assume that this process was associated to a crustal shortening period that probably terminated *c*. 22 Ma ago. This north–south shortening phase can be correlated to the D2 tectonic phase as defined by Godin (2003), Kellett & Godin (2009), and Antolin *et al.* (2011), or to the Neohimalayan phase of Hodges (2000).
  (4) *Miocene (between* c. *18 and 13 Ma).* The very base of the Tethyan Himalayan Sequence in the surroundings of the Yala Xiangbo dome experienced a greenschist-facies overprint. The formation of white micas or the cooling below their argon closure temperature took place *c*. 13 Ma, caused by the emplacement and exhumation of the Yala Xiangbo dome.

- Zircon and apatite (U–Th)/He ages indicate that the post-metamorphic cooling history lasted until Late Miocene times. The final cooling was not coeval in the whole THS, the northern zones experienced a later cooling probably induced by the exhumation of the hanging wall of the south-dipping Great Counter Thrust along its backthrust plane. The published thrusting ages of the MCT, STDS (see Godin *et al.* 2006) and GCT (Yin *et al.* 1994; Ratschbacher *et al.* 1994; Quidelleur *et al.* 1997; Harrison *et al.* 2000) suggest that these three tectonic structures where active during the same time interval.
- Methodologically, the present study showed the important role of the lithological constraints on the development of metamorphic minerals. The growth of white mica and garnet was hindered by high organic content and low permeability in the metapelites, while the meta-arenitic lithologies always contain much coarser and well-developed metamorphic minerals. Consequently, textures and sometimes even the paragenesis of meta-arenites and meta-tuffs indicate higher metamorphic conditions than the adjacent metapelites.

To Dr Péter Árkai who is not only a living index but also an always helpful mentor. The authors are grateful for the aid during fieldwork to our Tibetan drivers Puchum, Tawa, Nobu (Lhasa), and to the Chinese students Xu Xiaoxia, Xu Qiang and Zhang Qinghai (Beijing) who partly joined the field work. Many thanks for careful sample preparation to U. Grunewald and I. Ottenbacher (Göttingen). The final version of the manuscript was benefited by the helpful comments of two referees. This work was funded by the German Research Foundation (DFG) and is part of the Priority Programme 'Tibetan Plateau: Formation, Climate, Ecosystems (*TiP*)'.

References

Aikman, A., Harrison, T. M. & Lin, D. 2004. Preliminary results from the Yala-Xiangbo leucogranite dome, SE Tibet. *Himalayan Journal of Sciences*, **2**, 91.

Aikman, A., Harrison, T. M. & Lin, D. 2008. Evidence for early (>44 Ma) Himalayan crustal thickening, Tethyan Himalaya, southeastern Tibet. *Earth and Planetary Science Letters*, **274**, 14–23.

Antolin, B., Apell, E., Montomoli, C., Dunkl, I., Ding, L., Gloaguen, R. & El Bay, R. 2011. Kinematic evolution of the eastern Tethyan Himalaya: Constraints from magnetic fabric and structural properties of the Triassic flysch in SE Tibet. *In*: Poblet, J. & Lisle, R. (eds) *Kinematic Evolution and Structural Styles of Fold-and-Thrust Belts*. Geological Society, London, Special Publications, **349**, 99–121.

Árkai, P. 1991. Chlorite crystallinity: an empirical approach and correlation with illite crystallinity, coal rank and mineral facies as exemplified by Palaeozoic and Mesozoic rocks of northeast Hungary. *Journal of Metamorphic Geology*, **9**, 723–734.

Árkai, P., Faryad, S. W., Vidal, O. & Balogh, K. 2003. Very low-grade metamorphism of sedimentary rocks of the Meliata unit, Western Carpathians, Slovakia: implications of phyllosilicate characteristics. *International Journal of Earth Sciences*, **92**, 68–85.

Árkai, P., Sassi, F. P. & Desmons, J. 2007. Very low- to low-grade metamorphic rocks. *In*: Fettes, D. & Desmons, J. (eds) *Metamorphic Rocks: A Classification and Glossary of Terms: Recommendations of the International Union of Geological Sciences Subcommission on the Systematics of Metamorphic Rocks*. Cambridge University Press, Cambridge, UK, 36–42.

Armijo, R., Tapponnier, P., Mercier, J. L. & Tonglin, H. 1986. Quaternary extension in southern Tibet: field observations and tectonic implications. *Journal of Geophysical Research*, **91**, 13803–13872.

Armstrong, J. T. 1991. Quantitative elemental analysis of individual microparticles with electron beam instruments. *In*: Heinrich, K. F. J. & Newbury, D. E. (eds) *Electron Probe Quantification*. Plenum, New York, 261–315.

Barker, C. E. & Pawlewitcz, M. J. 1986. The correlation of vitrinite reflectance with maximum temperature in humic organic matter. *In*: Buntebarth, G. & Stegena, L. (eds) *Lecture Notes in Earth Sciences, Paleogeothermics*. Springer Verlag, **5**, 79–93.

Bostick, N. H. 1979. Microscopic measurement of the level of catagenesis of solid organic matter in sedimentary rocks to aid exploration for petroleum and to determine former burial temperatures – A review. *In*: Scholle, P. A. & Schluger, P. R. (eds) *Aspects of Diagenesis, Society of Economic Paleontologists and Mineralogists Special Publication*. Tulsa, Oklahoma, **26**, 17–44.

Brookfield, M. 1993. The Himalayan passive margin from Precambrian to Cretaceous. *Sedimentary Geology*, **84**, 1–35.

Burg, J. P. & Chen, G. M. 1984. Tectonics and structural zonation of southern Tibet, China. *Nature*, **311**, 219–223.

Carosi, R., Montomoli, C. & Visonà, D. 2007. A structural transect in the lower Dolpo: insights on the tectonic evolution of Western Nepal. *Journal of Asian Earth Sciences*, **29**, 407–423, doi: 10.1016/j.jseaes.2006.05.001.

Carosi, R., Montomoli, C., Rubatto, D. & Visonà, D. 2010. Late Oligocene high-temperature shear zones in the core of the higher Himalayan crystallines (Lower Dolpo, Western Nepal). *Tectonics*, doi: 10.1029/2008TC002400.

Catlos, E. J., Harrison, T. M., Manning, C. E., Grove, M., Rai, S. M., Hubbard, M. S. & Upreti, B. N. 2002. Records and evolution of the Himalayan orogen from in situ Th–Pb ion microprobe dating of monazite: eastern Nepal and western Garhwal. *Journal of Asian Earth Science*, **20**, 459–479.

Catlos, E. J., Dubey, C. S., Marston, R. A. & Harrison, M. T. 2007. Geochronological constraints across the main central thrust shear zone, Bhagirathi River (NW India): implications for Himalayan tectonics. *Geological Society of America Special Paper*, **419**, 135–150.

CLAUER, N. & CHAUDHURI, S. 1999. Isotopic dating of very low-grade metasedimentary and metavolcanic rocks: techniques and methods. *In*: FREY, M. & ROBINSON, D. (eds) *Low-grade Metamorphism*. Blackwell, Oxford, 202–226.

CONNOLLY, J. A. D. 2005. Computation of phase equilibria by linear programming: a tool for geodynamic modeling and its application to subduction zone decarbonation. *Earth and Planetary Science Letters*, **236**, 524–541.

CONNOLLY, J. A. D. & PETRINI, K. 2002. An automated strategy for calculation of phase diagram sections and retrieval of rock properties as a function of physical conditions. *Journal of Metamorphic Geology*, **20**, 697–708.

CROUZET, C., DUNKL, I., PAUDEL, L., ARKAI, P., RAINER, T. M., BALOGH, K. & APPEL, E. 2007. Temperature and age constraints on the metamorphism of the Tethyan Himalaya in Central Nepal: a multidisciplinary approach. *Journal of Asian Earth Sciences*, **30**, 113–130, doi: 10.1016/j.jseaes.2006.07.014.

DECELLES, P. G., ROBINSON, D. M., QUADE, J., OJHA, T. P., GARZIONE, C. N. & COPELAND, P. 2001. Stratigraphy, structure and tectonic evolution of the Himalayan fold-thrust belt in western Nepal. *Tectonics*, **20**, 487–509.

DING, L., KAPP, P. & WAN, X. 2005. Paleocene–Eocene record of ophiolite obduction and initial India–Asia collision, south central Tibet. *Tectonics*, **24**, TC3001, doi: 10.1029/2004TC001729.

DUPUIS, C., HÉBERT, R., DUBOIS-COTÉ, V., WANG, C. S., LI, Y. L. & LI, Z. J. 2005. Petrology and geochemistry of mafic rocks from mélange and flysch units adjacent to the Yarlung Zangbo suture zone, southern Tibet. *Chemical Geology*, **214**, 287–308.

DUPUIS, C., HÉBERT, R., DUBOIS-COTÉ, V., GUILMETTE, C., WANG, C. S. & LI, Z. J. 2006. Geochemistry of sedimentary rocks from mélange and flysch units south of the Yarlung Zangbo suture zone, southern Tibet. *Journal of Asian Earth Sciences*, **26**, 489–508.

EDWARDS, M. A. & HARRISON, T. M. 1997. When did the roof collapse? Late Miocene north–south extension in the high Himalaya revealed by Th–Pb monazite dating of the Khula Kangri granite. *Geology*, **25**, 543–546.

FARLEY, K. A., WOLF, R. A. & SILVER, L. T. 1996. The effects oflong alpha-stopping distance on (U–Th)/He ages. *Geochimica et Cosmochimica Acta*, **60**, 4223–4229.

FUCHS, G. 1967. *Zum Bau des Himalaya*. Österreichische Akademie der Wissenschaften, Mathematisch-Naturwissenschafliche Klasse, Denkschriften, **113**, 1–211.

FUHRMANN, U., LIPPOLT, H. J. & HESS, J. C. 1987. Examination of some proposed K–Ar standards: $^{40}Ar/^{39}Ar$ analyses and conventional K–Ar-Data. *Chemical Geology*, **66**, 41–51.

GAETANI, M. & GARZANTI, E. 1991. Multicyclic history of the northern Indian continental margin (northwestern Himalaya). *American Association of Petroleum Geologists, Bulletin*, **75**, 1427–1446.

GARZANTI, E. 1999. Stratigraphy and sedimentary history of the Nepal Tethys Himalaya passive margin. *Journal of Asian Earth Sciences*, **17**, 805–827.

GARZIONE, C. N., DECELLES, P. G., HODKINSON, D. G., OJHA, T. P. & UPRETI, B. N. 2003. East–west extension and Miocene environmental change in the southern Tibetan plateau: Thakkhola graben, central Nepal. *Geological Society of America Bulletin*, **115**, 3–20.

GODIN, L. 2003. Structural evolution of the Tethyan sedimentary sequence in the Annapurna area, central Nepal Himalaya. *Journal of Asian Earth Sciences*, **22**, 307–328.

GODIN, L., GRUJIC, D., LAW, R. D. & SEARLE, M. P. 2006. Channel flow, extrusion and exhumation in continental collision zones: an introduction. *In*: LAW, R. D., SEARLE, M. P. & GODIN, L. (eds) *Channel Flow, Ductile Extrusion and Exhumation in Continental Collision Zones*. Geological Society, London, Special Publications, **268**, 1–23.

GRUJIC, D., LINCOLN, S., HOLLISTER, L. S. & PARRISH, R. R. 2002. Himalayan metamorphic sequence as an orogenic channel: insight from Bhutan. *Earth and Planetary Science Letters*, **198**, 177–191.

GUILLOT, S., PÊCHER, A., ROCHETTE, P. & LEFORT, P. 1993. The emplacement of the Manaslu granite of central Nepal: field and magnetic susceptibility constraints. *In*: TRELOAR, P. J. & SEARLE, M. P. (eds) *Himalayan Tectonics*. Geological Society, London, Special Publications, **74**, 413–428.

GUILLOT, S., GARZANTI, G., BARATOUX, D., MARQUER, D., MAHEO, G. & DE SIGOYER, J. 2003. Reconstructing the total shortening history of the NW Himalaya. *Geochemistry, Geophysics, Geosystems*, **4**, 1064 doi: 10.1029/2002GC000484.

HARRISON, T. M., RYERSON, F. J., LE FORT, P., YIN, A., LOVERA, O. M. & CATLOS, E. J. 1997. A late Miocene–Pliocene origin for the Central Himalayan inverted metamorphism. *Earth and Planetary Science Letters*, **146**, E1–E8.

HARRISON, T. M., YIN, A., GROVE, M. & LOVERA, O. M. 2000. The Zedong Window: a record of superposed Tertiary convergence in southeastern Tibet. *Journal of Geophysical Research*, **105**, 19,211–19,320.

HEIM, A. & GANSSER, A. 1939. Central Himalaya. Geological observations of the Swiss expedition 1936. *Mémoires de la Société Helvétique des Sciences Naturelles*, **7/31**, 1–245.

HEINRICHS, H. & HERRMANN, A. G. 1990. *Praktikum der Analytischen Geochemie*. Springer Verlag, Berlin.

HODGES, K. V., PARRISH, R. R. & SEARLE, M. P. 1996. Tectonic evolution of the central Annapurna Range, Nepalese Himalayas. *Tectonics*, **15**, 1264–1291.

HODGES, K. V. 2000. Tectonics of the Himalaya and southern Tibet from two perspectives. *Geological Society of America Bulletin*, **112**, 324–350.

HOLLAND, T. J. B. & POWELL, R. 1998. An internally-consistent thermodynamic dataset for phases of petrological interest. *Journal of Metamorphic Geology*, **16**, 309–344.

HOWER, J., HURLEY, P. M., PINSON, W. H. & FAIRBAIRN, H. W. 1963. The dependence of K–Ar age on the mineralogy of various particle size ranges in a shale. *Geochimica et Cosmochimica Acta*, **27**, 405–410.

HURLEY, P. M., HUNT, J. M., PINSON, W. H. & FAIRBAIRN, H. W. 1963. K–Ar age values on the clay fractions in dated shales. *Geochimica et Cosmochimica Acta*, **27**, 279–284.

Jadoul, F., Berra, F. & Garzanti, E. 1998. The Tethys Himalayan passive margin from Late Triassic to Early Cretaceous (South Tibet). *Journal of Asian Earth Sciences*, **16**, 173–198.

Judik, K., Rantitsch, G., Rainer, Th. M., Árkai, P. & Tomljenović, B. 2008. Organic metamorphism in metasedimentary rocks from Mt. Medvednica (Croatia). *Swiss Journal of Geosciences*, **101**, 605–616.

Kellett, D. A & Godin, L. 2009. Pre-Miocene deformation of the Himalayan superstructure, Hidden valley, central Nepal. *Journal of the Geological Society, London*, **166**, 261–275.

Kisch, H. J., Árkai, P. & Brime, C. 2004. On the calibration of the illite Kübler index (illite 'crystallinity'). *Schweizerische Mineralogische und Petrographische Mitteilungen*, **84**, 323–331.

Kohn, M. J. & Spear, F. S. 1991. Error propagation for barometers: 1. Accuracy and precision of experimentally located end-member reactions. *American Mineralogist*, **76**, 128–137.

Kübler, B. 1967. La cristallinité de l'illite et les zones tout à fait supérieures du métamorphisme. *Étages Tectoniques*, Colloque de Neuchâtel 1966. Edition de la Baconnière, Neuchâtel, 105–122.

Kübler, B. 1968. Evaluation quantitative du metamorphisme par la cristallinité de l'illite. *Bulletin du Centre de Recherches, Pau SNPA*, **2**, 385–397.

Kübler, B. 1990. 'Cristallinité' de l'illite et mixed-layers: brève révision. *Schweizerische Mineralogische und Petrographische Mitteilungen*, **70**, 89–93.

Le Fort, P. 1971. *Les formations cristallophyliennes de la Thakkhola. Recherches géologiques dans l'Himalaya du Népal, région del Thakkhola*. Edition du CNRS, Paris.

Le Fort, P. 1975. Himalayas, the collided range. Present knowledge of the continental arc. *American Journal of Science*, **275-A**, 1–44.

Lee, J., Hacker, B. R. *et al.* 2000. Evolution of the Kangmar Dome, southern Tibet: structural, petrologic, and thermochronologic constraints. *Tectonics*, **19**, 872–895.

Leech, M. L. 2008. Does the Karakoram fault interrupt mid-crustal channel flow in the western Himalaya? *Earth and Planetary Science Letters*, **276**, 314–322.

Liu, G. & Einsele, G. 1994. Sedimentary history of the Tethyan basin in the Tibetan Himalayas. *Geologische Rundschau*, **83**, 32–61.

Livi, K. J. T., Veblen, D. R., Ferry, J. M. & Frey, M. 1997. Evolution of 2:1 layered silicates in low-grade metamorphosed Liassic shales of Central Switzerland. *Journal of Metamorphic Geology*, **15**, 323–344.

McQuarrie, N., Robinson, D., Long, S., Tobgay, T., Grujic, D., Gehrels, G. & Ducea, M. 2008. Preliminary stratigraphic and structural architecture of Bhutan: implications for the along strike architecture of the Himalayan system. *Earth and Planetary Science Letters*, **272**, 105–117.

Mercier, J. L. *et al.* 1984. La collision Inde-Asie côté Tibet. *In*: Mercier, J. L. & Li, G. C. (eds) *Mission Franco-Chinoise Au Tibet 1980: Étude Géologique Et Géophysique De La Croûte Terrestre Et Du Manteau Supérieur Du Tibet Et De ĹHimalaya*. Editions du Centre National de la Recherche Scientifique, Paris, France, **29**, 341–350.

Meunier, A. & Velde, B. 2004. *Illite: Origins, Evolution and Metamorphism*. Springer, 286.

Montomoli, C., Appel, E., Antolin, B., Dunkl, I., El Bay, R., Lin, D. & Gloaguen, R. 2008. Polyphase deformation history of the 'Tibetan sedimentary sequence' in the Himalaya chain (South-East Tibet). *Himalayan Journal of Sciences*, **5**, 91.

Najman, Y., Carter, A., Oliver, G. & Garzanti, E. 2005. Provenance of Eocene foreland basin sediments, Nepal: constraints to the timing and diachroneity of early Himalayan orogenesis. *Geology*, **33**, 309–312.

Pan, G., Ding, J., Yao, D. & Wang, L. 2004. *Geological map of Qinghai-Xizang (Tibet) Plateau and Adjacent Areas (1:1,500,000)*. Chengdu Institute of Geology and Mineral Resources, China Geological Survey. Chengdu Cartographic Publishing House.

Patzelt, A., Li, H., Wang, J. & Appel, E. 1996. Paleomagnetism of Cretaceous to Tertiary sediments from southern Tibet: evidence for the extent of the northern margin of India prior to the collision with Eurasia. *Tectonophysics*, **259**, 259–284.

Paudel, L. P. & Arita, K. 2006. Thermal evolution of the Lesser Himalaya, central Nepal: insights from K-white micas compositional variation. *Gondwana Research*, **9**, 409–425.

Pêcher, A. 1975. The Main Central Thrust of the Nepal Himalaya and the related metamorphism in the Modi Khola cross-section (Annapurna Range). *Himalayan Geology*, **5**, 115–131.

Potel, S. 2007. Very low-grade metamorphic study in the pre-Late Cretaceous terranes of New Caledonia (southwest Pacific Ocean). *Island Arc*, **16**, 291–305.

Powell, R. & Holland, T. J. B. 1994. Optimal geothermometry and geobarometry. *American Mineralogist*, **79**, 120–130.

Powell, R. & Holland, T. J. B. 2006. Course Notes for 'THERMOCALC Short Course'. Sao Paulo, Brazil, on CD-ROM.

Powell, R. & Holland, T. J. B. 2008. On thermobarometry. *Journal of Metamorphic Geology*, **26**, 155–179.

Quidelleur, X., Grove, M., Lovera, O. M., Harrison, T. M. & Yin, A. 1997. Thermal evolution and slip history of the Renbu-Zedong thrust, southeastern Tibet. *Journal of Geophysical Research*, **102**, 2659–2679.

Ratschbacher, L., Frisch, W., Liu, G. & Chen, C. 1994. Distributed deformation in southern and western Tibet during and after the India–Asia collision. *Journal of Geophysical Research*, **99**, 19,917–19,945.

Reuter, A. 1987. Implications of K–Ar ages of whole-rock and grain-size fractions of metapelites and intercalated metatuffs within an anchizonal terrane. *Contribution to Mineralogy and Petrology*, **97**, 105–115.

Robinson, D. M., DeCelles, P. G., Garzione, C. N., Pearson, O. N., Harrison, T. M. & Catlos, E. J. 2003. Kinematic model for the Main Central thrust in Nepal. *Geology*, **31**, 339–362.

Schumacher, E. 1975. Herstellung von 99,9997% ^{38}Ar für die ^{40}K/^{40}Ar Geo-chronologie. *Geochronologia Chimia*, **24**, 441–442.

Searle, M. 1986. Structural evolution and sequence of thrusting in the High Himalayan, Tibetan-Tethys and Indus suture zones of Zanskar and Ladakh, Western Himalaya. *Journal of Structural Geology*, **8**, 923–936.

SEARLE, M. P. & GODIN, L. 2003. The south Tibetan detachment and the Manaslu leucogranite: a structural reinterpretation and restoration of the Annapurna-Manaslu Himalaya, Nepal. *Journal of Geology*, **111**, 505–523.

SPEAR, F. S. 1995. *Metamorphic Phase Equilibria and Pressure–Temperature–Time Paths*. Mineralogical Society of America, Washington DC, 1–799.

STEIGER, R. H. & JÄGER, E. 1977. Subcommission on geochronology: convention on the use of decay constants in geo- and cosmochronology. *Earth and Planetary Science Letters*, **36**, 359–362.

STÖCKLIN, J. 1980. Geology of Nepal and its regional frame. *Journal of the Geological Society, London*, **137**, 1–34.

SWEENEY, J. J. & BURNHAM, A. K. 1990. Evaluation of a simple model of vitrinite reflectance based on chemical kinetics. *Bulletin American Association of Petroleum Geologists*, **74**, 1559–1570.

UPRETI, B. N. 2001. Stratigraphy, structure, and tectonic evolution of the Himalayan fold-thrust belt in western Nepal. *Tectonics* **20**, 487–509.

VALDIYA, K. S. 1980. *Geology of the Kumaun Lesser Himalaya*. Wadia Institute of Himalayan Geology, Dehra Dun.

WARR, L. N. & RICE, A. H. N. 1994. Interlaboratory standardisation and calibration of clay mineral crystallinity and crystallite size data. *Journal of Metamorphic Geology*, **12**, 141–152.

WEMMER, K. 1991. K/Ar-Altersdatierungsmöglichkeiten für retrograde Deformationsprozesse im spröden und duktilen Bereich – Beispiele aus der KTB-Vorbohrung (Oberpfalz) und dem Bereich der Insubrischen Linie (N-Italien). *Göttinger Arbeiten zur Geologie und Paläontologie*, **51**, 1–61.

WILLEMS, H., ZHOU, Z., ZHANG, B. & GRÄFE, K. U. 1996. Stratigraphy of the Upper Cretaceous and lower Tertiary strata in the Tethyan Himalayas of Tibet (Tingri area, China). *Geologische Rundschau*, **85**, 723–754.

WOJDYR, M. 2007. *FITYK: A curve fitting and data analysis program*. World Wide Web address: http://www.unipress.waw.pl/fityk/

XU, X., DING, L., QIANG, X., FULONG, C., QINGHAI, Z., LIYUN, Z. & QINGZHOU, L. 2009. Tectonic implications of the Ultramafic Dykes in Southeastern Tibet. *Chinese Journal of Geology*, **44**, 1012–1024.

YIN, A. 2006. Cenozoic tectonic evolution of the Himalayan orogen as constrained by along–strike variation of structural geometry, exhumation history, and foreland sedimentation. *Earth-Science Reviews*, **76**, 1–131.

YIN, A., HARRISON, T. M., RYERSON, F. J., WENJI, C., KIDD, W. & COPELAND, P. 1994. Tertiary structural evolution of the Gangdese thrust system, southeastern Tibet. *Journal of Geophysical Research*, **99**, 18, 175–18, 201.

ZHU, D., MO, X. *ET AL*. 2008. Petrogenesis of the earliest Early Cretaceous mafic rocks from the Cona area of the eastern Tethyan Himalaya in south Tibet: interaction between the incubating Kerguelen plume and the eastern Greater India lithosphere? *Lithos*, **100**, 147–173.